

2D Materials

OPEN ACCESS



PAPER

RECEIVED

30 March 2017

REVISED

7 June 2017

ACCEPTED FOR PUBLICATION

19 June 2017

PUBLISHED

1 September 2017

Original content from this work may be used under the terms of the [Creative Commons Attribution 3.0 licence](https://creativecommons.org/licenses/by/3.0/).

Any further distribution of this work must maintain attribution to the author(s) and the title of the work, journal citation and DOI.



The structural phases and vibrational properties of $\text{Mo}_{1-x}\text{W}_x\text{Te}_2$ alloys

Sean M Oliver^{1,4}, Ryan Beams^{2,4}, Sergiy Krylyuk^{2,3}, Irina Kalish², Arunima K Singh², Alina Bruma², Francesca Tavazza², Jaydeep Joshi¹, Iris R Stone¹, Stephan J Stranick², Albert V Davydov² and Patrick M Vora^{1,5}

¹ Department of Physics and Astronomy, George Mason University, Fairfax, VA 22030, United States of America

² Material Measurement Laboratory, National Institute of Standards and Technology, Gaithersburg, MD 20899, United States of America

³ Theiss Research, La Jolla, CA 92037, United States of America

⁴ These authors contributed equally to the work

⁵ Author to whom correspondence should be addressed

E-mail: pvora@gmu.edu

Keywords: transition metal dichalcogenides, alloys, Raman spectroscopy, phase transition, disorder, x-ray diffraction, polarization

Supplementary material for this article is available [online](#)

Abstract

The structural polymorphism in transition metal dichalcogenides (TMDs) provides exciting opportunities for developing advanced electronics. For example, MoTe_2 crystallizes in the 2H semiconducting phase at ambient temperature and pressure, but transitions into the $1T'$ semimetallic phase at high temperatures. Alloying MoTe_2 with WTe_2 reduces the energy barrier between these two phases, while also allowing access to the T_d Weyl semimetal phase. The $\text{Mo}_{1-x}\text{W}_x\text{Te}_2$ alloy system is therefore promising for developing phase change memory technology. However, achieving this goal necessitates a detailed understanding of the phase composition in the MoTe_2 - WTe_2 system. We combine polarization-resolved Raman spectroscopy with x-ray diffraction (XRD) and scanning transmission electron microscopy (STEM) to study bulk $\text{Mo}_{1-x}\text{W}_x\text{Te}_2$ alloys over the full compositional range x from 0 to 1. We identify Raman and XRD signatures characteristic of the 2H, $1T'$, and T_d structural phases that agree with density-functional theory (DFT) calculations, and use them to identify phase fields in the MoTe_2 - WTe_2 system, including single-phase 2H, $1T'$, and T_d regions, as well as a two-phase $1T' + T_d$ region. Disorder arising from compositional fluctuations in $\text{Mo}_{1-x}\text{W}_x\text{Te}_2$ alloys breaks inversion and translational symmetry, leading to the activation of an infrared $1T'$ - MoTe_2 mode and the enhancement of a double-resonance Raman process in 2H- $\text{Mo}_{1-x}\text{W}_x\text{Te}_2$ alloys. Compositional fluctuations limit the phonon correlation length, which we estimate by fitting the observed asymmetric Raman lineshapes with a phonon confinement model. These observations reveal the important role of disorder in $\text{Mo}_{1-x}\text{W}_x\text{Te}_2$ alloys, clarify the structural phase boundaries, and provide a foundation for future explorations of phase transitions and electronic phenomena in this system.

1. Introduction

Transition metal dichalcogenides (TMDs) are van der Waals (vdW) compounds that follow the general formula of MX_2 , where M is a transition metal from Groups IVB–VIB, and X is a Group VIIA chalcogen, such as S, Se, and Te. This chemical versatility leads to unique electronic properties, such as semiconducting behavior [1], superconductivity [2–4], and topological electronic states [5–8]. Furthermore, two-dimensional

(2D) TMD monolayers can be vertically stacked without the need for lattice matching, which allows these dissimilar electronic phases to be combined in a single heterostructure [9].

The chemical versatility intrinsic to TMDs and the novel interactions achieved through vdW stacking are complimented further by the structural polymorphism of TMDs. A prototypical example is molybdenum ditelluride (MoTe_2), which can be grown in a semiconducting 2H phase (space group $P6_3/mmc$) or a semimetallic $1T'$ phase

(space group $P2_1/m$) [10–12]. The hexagonal 2H phase, characterized by a trigonal prismatic coordination, is thermodynamically stable under ambient conditions, while the monoclinic $1T'$ phase is stable above 900 °C. The $1T'$ phase can be stabilized at room temperature by rapid cooling [13], control of the tellurization rate of Mo films [10], or choosing appropriate precursors for chemical vapor deposition [14, 15]. When cooled below ~ 250 K, $1T'$ - MoTe_2 transitions into an orthorhombic T_d phase (space group $Pmn2_1$) with broken inversion symmetry as evidenced by electrical, structural, and optical measurements [11, 16–18].

Interest in MoTe_2 has surged due to the unique electronic properties of its structural phases as well as the possibility of engineering controlled transitions between these phases. For instance, type-II Weyl semimetal states were theoretically predicted and experimentally observed in both T_d - MoTe_2 and T_d - WTe_2 [6, 7, 19–23]. The broken inversion symmetry of the T_d phase is a necessary condition for the type-II Weyl state [6, 19, 20] and allows for fundamental studies of interesting topological physics. However, efforts to directly observe the Weyl state using angle-resolved photoemission spectroscopy are frustrated by the presence of overlapping band-crossings and insufficient experimental resolution [20]. A more practical application driving investigations of MoTe_2 is the development of atomically thin phase change memory. MoTe_2 has a small energy difference between the 2H and $1T'$ phases, making the prospect of engineering on-demand transitions with low power consumption realistic [24–28]. Unfortunately, reversible and rapid phase changes in MoTe_2 have yet to be demonstrated. This may suggest that the energy difference between the 2H and $1T'$ phases must be reduced further in order to successfully perform phase change operations.

The limitations of MoTe_2 highlighted above can be addressed by alloy engineering. Substitutional doping of Mo with W atoms results in $\text{Mo}_{1-x}\text{W}_x\text{Te}_2$ alloys which have properties advantageous for both fundamental investigations and practical applications. $\text{Mo}_{1-x}\text{W}_x\text{Te}_2$ alloys have been theoretically predicted [20] and experimentally confirmed [29] to be type-II Weyl semimetals. Importantly, the separation of the Weyl nodes in the alloys can be tuned with composition [20], which facilitates the observation of topological electronic states. Additionally, the ground state energy difference between the semiconducting 2H and semimetallic $1T'$ or T_d phases in $\text{Mo}_{1-x}\text{W}_x\text{Te}_2$ alloys can also be tuned with composition [25, 27], thereby reducing the energy required to trigger a semiconductor-semimetal phase transformation. The desirable combination of tunable phase transitions with the low-dimensionality of TMDs makes $\text{Mo}_{1-x}\text{W}_x\text{Te}_2$ highly promising for phase change memory applications.

Application of the $\text{Mo}_{1-x}\text{W}_x\text{Te}_2$ alloy system in the 2D limit necessitates an understanding of the compositional dependence of phase transformations and the impact of disorder upon the bulk material properties. The literature on this subject is very limited. In a pioneering work on $\text{Mo}_{1-x}\text{W}_x\text{Te}_2$ polycrystalline

powders, Revolinsky and Beerntsen found that the alloys crystallize in the 2H phase for $x \leq 0.15$, the T_d phase for $x \geq 0.65$, and a two-phase region of $2H + T_d$ in between [30]. On the contrary, Champion detected a two-phase $2H + T_d$ region only for $x = 0.25$ composition, whereas a higher (lower) W content resulted in $\text{Mo}_{1-x}\text{W}_x\text{Te}_2$ powders in a T_d (2H) phase, respectively [31]. However, no detailed structural studies were reported in these two papers to shed light on the co-existence of the 2H and T_d phases, especially considering a noticeable difference in their symmetry. Recently, Rhodes *et al* reported a simplified phase diagram without two-phase regions for single-crystalline $\text{Mo}_{1-x}\text{W}_x\text{Te}_2$ alloys grown by the chemical vapor transport method (CVT) with iodine or TeCl_4 as the transport agent [32]. Finally, Lv *et al* and Yan *et al* suggested a more complicated phase diagram with a mixed $1T' + T_d$ region that exists for compositions $0.5 < x < 0.7$ in $\text{Mo}_{1-x}\text{W}_x\text{Te}_2$ alloys also grown using CVT, but with Br_2 as the transport agent [33, 34]. This significant disagreement between the studies about phase boundaries between the phases in the MoTe_2 - WTe_2 system, combined with the absence of thorough studies of compositional disorder on optical properties, calls for a fresh look at this alloy system.

Here, we provide a comprehensive examination of the $\text{Mo}_{1-x}\text{W}_x\text{Te}_2$ alloy system by combining x-ray diffraction (XRD), scanning transmission electron microscopy (STEM), density-functional theory (DFT), and polarization-resolved Raman spectroscopy to explore the properties of the $1T'$, T_d , and 2H structural phases in bulk $\text{Mo}_{1-x}\text{W}_x\text{Te}_2$ crystals grown by iodine-assisted CVT. Measurement of bulk flakes has the added advantage of minimizing the well-known degrading oxidation effects of Te-based TMDs [35]. XRD and STEM measurements indicate that the $\text{Mo}_{1-x}\text{W}_x\text{Te}_2$ alloys with the $1T'$ crystal structure are stable at elevated temperatures with W content $x \leq 0.04$, while alloys with the T_d structure are stable for $x \geq 0.63$. The alloys with intermediate compositions $0.04 < x < 0.63$ form a two-phase, $1T' + T_d$, mixture. Polarized Raman measurements offer further insight into the transition from $1T'$ to the two-phase, $1T' + T_d$, field and ultimately to the T_d single-phase region as a function of x . We use Raman tensor analysis to assign the phonon mode symmetry for all compositions and find that the tensor elements must be complex in order to capture the polarization dependence. This observation is consistent with prior studies of MoTe_2 [18, 36] as well as studies of other layered TMD materials [37]. The Raman peaks for certain phonon modes show particular sensitivity to x and lattice symmetry. For example, the Raman peak at 128 cm^{-1} for the $1T'$ - $\text{Mo}_{1-x}\text{W}_x\text{Te}_2$ alloys broadens at $x = 0.09$ and splits into a doublet for compositions $x \geq 0.29$, which implies a loss of inversion symmetry [18] due to the substitution of Mo by W. We also observe the activation of a new Raman mode at 178 cm^{-1} that is unique to $0.02 < x < 1$ alloys. Based on our DFT calculations, we assign this feature as a

disorder-activated infrared mode in MoTe₂. Furthermore, the separation between the two modes near 260 cm⁻¹ in MoTe₂ is highly composition-dependent and can be used to infer x . In 2H-Mo_{1-x}W_xTe₂, we observe minor changes in the A_{1g} and E_{2g}¹ mode frequencies, linewidths, and relative intensities. We also identify a new Raman mode at 202 cm⁻¹ that originates from a double-resonance Raman process [38] and is apparently enhanced by alloy disorder. The comprehensive structural and spectroscopic data assembled here provide an important roadmap for the future study and application of 2D Mo_{1-x}W_xTe₂ alloys.

2. Methods

Polycrystalline Mo_{1-x}W_xTe₂ alloys ($x = 0...1$) were prepared by reacting stoichiometric amounts of molybdenum (99.999%), tungsten (99.9%), and tellurium (99.9%) powders at 750 °C in vacuum-sealed quartz ampoules. Mo_{1-x}W_xTe₂ crystals were then grown by the CVT method using approximately 1.5 g of poly-Mo_{1-x}W_xTe₂ charge and a small amount of iodine (99.8%, 5 mg cm⁻¹³) sealed in evacuated quartz ampoules. It was found that the temperature required for high-yield synthesis of Mo_{1-x}W_xTe₂ crystals is lower for higher x . Therefore, the growth temperatures used in this study were 1000 °C for $x \leq 0.12$, 950 °C for $0.12 < x \leq 0.63$, and 900 °C for $x \geq 0.71$. The ampoules were ice-water quenched after 7 d of growth. To study phase transformation in Mo_{1-x}W_xTe₂, as-grown crystals were vacuum-sealed in small ampoules (internal volume ≈ 1 cm³) and annealed at 750 °C for 72 h followed by cooling to room temperature at a rate of 10 °C/hr.

Chemical compositions with an accuracy of 0.01 were determined by energy-dispersive x-ray spectroscopy (EDS) using a JEOL JSM-7100F field emission scanning electron microscope (FESEM) equipped with an Oxford Instruments X-Max 80 EDS detector⁶. We examined the θ - 2θ XRD patterns derived from a Norelco Philips Diffractometer with the Bragg-Brentano geometry. Lattice parameters were refined using the MDI-JADE 6.5 software package. For the powder XRD study, Mo_{1-x}W_xTe₂ crystals were finely ground using an agate mortar. An Aberration-Corrected High Angle Annular Dark Field Scanning Transmission Electron Microscopy (Cs-corrected HAADF-STEM) FEI Titan 80-300 TEM/STEM operating at 300 kV was employed for the characterization of Mo_{1-x}W_xTe₂ samples. The flakes were crushed in ethanol and a drop of solution was deposited onto an amorphous Carbon (a-C) coated TEM grid (Agar Inc.). HAADF-STEM

⁶ Disclaimer: certain commercial equipment, instruments, or materials are identified in this paper in order to specify the experimental procedure adequately. Such identification is not intended to imply recommendation or endorsement by the National Institute of Standards and Technology, nor is it intended to imply that the materials or equipment identified are necessarily the best available for the purpose.

images were collected at a camera length of 100 mm corresponding to inner and outer collection angles of 70.6 and 399.5 mrad respectively.

For Raman measurements, the as-grown Mo_{1-x}W_xTe₂ crystals were mechanically exfoliated onto Si/SiO₂ substrates. Polarization-dependent Raman measurements were performed on bulk flakes in a back-scattering geometry at room temperature in atmosphere using a linearly-polarized 532 nm continuous wave laser. The polarization of the excitation beam was controlled with a motorized achromatic half-wave plate and was focused onto the sample using a 0.75 NA microscope objective. The back-scattered Raman emission was collected by the same objective, and then sent through a motorized analyzer and a long-pass filter. The excitation polarization and collection analyzer were oriented in both co-polarized (||) and cross-polarized (\perp) configurations, and then rotated together while the sample remained fixed. The filtered light was focused into a multimode fiber to scramble polarization and then directed to a spectrometer for analysis. Raman peaks were fit to Lorentzian functions to extract mode frequencies, linewidths, and amplitudes. For angle-dependent Raman maps, measurements were normalized by the feature with the greatest intensity, the ~ 163 cm⁻¹ peak. The angle-dependent peak intensities were fit using the Raman tensors to assign peak symmetries.

All simulations were based on density-functional theory (DFT) using the projector-augmented wave method as implemented in the plane-wave code VASP [39]. The simulations were performed using the vdW-DF-optB88 exchange-correlation functional [40], which provides an excellent description of the lattice constants of bulk 1T'-MoTe₂, T_d-MoTe₂, and T_d-WTe₂. An energy cutoff of 600 eV and k-point mesh of $10 \times 18 \times 5$ for the $1 \times 1 \times 1$ unit cells of bulk 1T'-MoTe₂, T_d-MoTe₂, and T_d-WTe₂ resulted in an accuracy of the total energies of 1 meV/unit cell. The 5s²5p⁴ and 4d⁵5s electrons were considered as the valence electrons for Te and Mo, respectively. Including the semicore 4s²4p⁶ electrons for Mo had a negligible effect on the results, as, for instance, the lattice parameters of bulk 1T'-MoTe₂ changed by less than 10%. Γ -point phonon frequencies of bulk 1T'-MoTe₂, T_d-MoTe₂, and T_d-WTe₂ were estimated from density-functional perturbation theory simulations of the $1 \times 1 \times 1$ unit cells of respective materials. Irreducible representations of normal modes were obtained from the PHONOPY program [41] and the Bilbao Crystallographic Server [42]. The phonon dispersion of T_d-WTe₂ in the entire Brillouin zone was estimated by computing normal mode frequencies on a uniform three-dimensional mesh of $51 \times 51 \times 51 \vec{q}$ -points between (0, 0, 0) and $(2\pi/a, 2\pi/b, 2\pi/c)$ (figure S1 in the supporting information (stacks.iop.org/TDM/4/045008/mmedia)). The phonon dispersion of T_d-WTe₂ in the entire Brillouin zone was computed using the finite difference method on the 106 atom $3 \times 3 \times 1$ supercell.

3. Results and discussion

Figure 1(a) summarizes heat-treatment schedules, compositions, and crystal phases of $\text{Mo}_{1-x}\text{W}_x\text{Te}_2$ ($x = 0 \dots 1$) samples examined in this study. The high-temperature phases of the alloys were preserved by quenching of the growth ampoules in an ice-water bath. This process is known to prevent reversal of the $1\text{T}'$ phase to the 2H phase, which is thermodynamically stable in MoTe_2 under ambient conditions [43]. Notably, XRD θ - 2θ scans from the as-grown, un-milled $\text{Mo}_{1-x}\text{W}_x\text{Te}_2$ flakes produce only $00l$ -type reflections and miss all asymmetric reflections, thus limiting the ability to reliably determine phase composition in the alloys. Therefore, we collected the scans from finely ground flakes to register all possible hkl reflections to distinguish $1\text{T}'$, T_d , and 2H phases and their mixtures. For example, R. Clarke *et al* have established that a $1\text{T}' \rightarrow \text{T}_d$ transition in MoTe_2 and the two-phase region can be observed by specifically monitoring $h0l$ reflections as a function of temperature, e.g. $\bar{1}012$ and 1012 reflections of $1\text{T}'$ - MoTe_2 coalesce into a single 1012 reflection of the low-temperature T_d phase [17]. A similar approach was applied to construct a phase diagram of $\text{Mo}_{1-x}\text{Nb}_x\text{Te}_2$ alloys that undergo an orthorhombic to monoclinic phase transition with increasing x [44].

The θ - 2θ scans of three representative $\text{Mo}_{1-x}\text{W}_x\text{Te}_2$ samples with $x = 0.04, 0.33,$ and 0.71 , produced by milling as-grown flakes in an agate mortar, are shown in figure 1(b). Figures 1(c) and (d) show enlarged portions of the scans around 2θ angles of 35° and 48° , respectively, which illustrate the distinct changes in the lineshape with increasing x . The scans for $x = 0.04$ and 0.71 were unambiguously assigned to the $1\text{T}'$ and T_d phase, respectively. The $x = 0.33$ scan can only be fitted by combining reflections from both $1\text{T}'$ and T_d phases, which indicates a two-phase coexistence. Calculated lattice parameters, Bragg reflection angles for the three samples, and a detailed explanation of the protocol used for identifying structural phases are presented in tables S1, S2, and supporting note 1 in the supporting information. By analysis of the powder XRD scans, we established that the quenched $\text{Mo}_{1-x}\text{W}_x\text{Te}_2$ alloy samples synthesized in this study are in the monoclinic $1\text{T}'$ phase for $x \leq 0.04$, the orthorhombic T_d phase for $x \geq 0.63$, and in the $1\text{T}' + \text{T}_d$ two-phase state for the compositions x between 0.04 and 0.63 .

We further verified these observations by performing HAADF-STEM measurements of $1\text{T}'$ - $\text{Mo}_{0.96}\text{W}_{0.04}\text{Te}_2$ and T_d - $\text{Mo}_{0.29}\text{W}_{0.71}\text{Te}_2$ crystals, shown in figures 1(e) and (f) with the overlapped atomic models and their corresponding fast fourier transforms (FFT) in the insets. Both the $1\text{T}'$ and the T_d phases exhibit a ‘buckled’ structure with visible shifts for Te atoms and a zig-zag pattern for Mo/W atoms. The presence of the two phases was observed on a sample with $x = 0.33$, proving the $1\text{T}' + \text{T}_d$ coexistence in $\text{Mo}_{1-x}\text{W}_x\text{Te}_2$ alloys

for $0.04 < x < 0.63$, although we were not able to map the spatial distribution of $1\text{T}'$ and T_d phases.

In order to study temperature-induced phase transformations in $\text{Mo}_{1-x}\text{W}_x\text{Te}_2$ alloys, the samples were annealed in vacuum-sealed ampoules at 750°C for 72 h followed by slow cooling to room temperature (squares in figure 1(a)). We found that alloys with $x \leq 0.09 \pm 0.01$ could be converted to the hexagonal 2H phase, as schematically depicted in figure 1(a) by the pink-colored area. HAADF-STEM and XRD data of the $\text{Mo}_{0.91}\text{W}_{0.09}\text{Te}_2$ sample converted from $1\text{T}'$ into 2H phase are provided in figure S2 of the supporting information. The vacuum annealing did not change the crystal structures of the alloys with larger x . Thus, an upper limit for $\text{Mo}_{1-x}\text{W}_x\text{Te}_2$ alloys to experience a reversible phase transformation between semiconducting 2H and metallic $1\text{T}'$ phases is $x \approx 0.09$. Approximately the same boundary between metallic and semiconducting phases was recently reported for $\text{Mo}_{1-x}\text{W}_x\text{Te}_2$ alloys [32, 33]. Additional studies are required to determine compositional dependencies of the phase transition temperatures in $\text{Mo}_{1-x}\text{W}_x\text{Te}_2$ alloys, which are beyond the scope of this paper.

We now investigate the impact of composition, disorder, and crystal structure on the Raman-active phonon modes of $\text{Mo}_{1-x}\text{W}_x\text{Te}_2$ alloys. We first examine the $1\text{T}' \rightarrow \text{T}_d$ phase transition in $\text{Mo}_{1-x}\text{W}_x\text{Te}_2$, and then explore the impact of alloy potential fluctuations on the 2H phase. In order to minimize rapid degradation of the detected Raman signal due to surface oxidation of Te-based TMD layers in air [35], we focus exclusively on bulk $\text{Mo}_{1-x}\text{W}_x\text{Te}_2$ flakes that are mechanically exfoliated onto Si substrates with a 285 nm SiO_2 layer. Future measurements will assess layer-dependent properties, but will require exfoliation and encapsulation in an inert environment. The home-built confocal Raman microscope used in these measurements is oriented in a backscattering geometry and operated in two polarization configurations: one with the excitation polarization and analyzer co-polarized (\parallel) and the other with them cross-polarized (\perp). The excitation/analyzer orientation is fixed and the two are rotated together relative to the crystal lattice. All measurements are performed at room temperature in atmosphere on bulk flakes. By acquiring a series of these spectra at different orientations, we assemble polarized Raman maps that provide a concise visualization of the angle-dependent Raman spectra as a function of x , which are shown for all $1\text{T}'$ and T_d samples in figure S3 of the supporting information. Due to our experimental geometry, only A_g (A_1) and B_g (A_2) symmetry modes are accessible for the $1\text{T}'$ (T_d) crystal structure. These modes have distinct dependencies on laser-analyzer orientation and the orientation relative to the crystal axes [36, 45]. In short, the polarized Raman signal is given by $I(\theta) = |\hat{\epsilon}_s \cdot \vec{R}\hat{\epsilon}_i|^2$, where $\hat{\epsilon}_i$ and $\hat{\epsilon}_s$ are the incident and scattered fields and \vec{R} is the Raman tensor. In bulk MoTe_2 and WTe_2 , \vec{R} is complex-valued for all modes, suggesting that optical absorption is significant [36, 46, 47]. We summarize

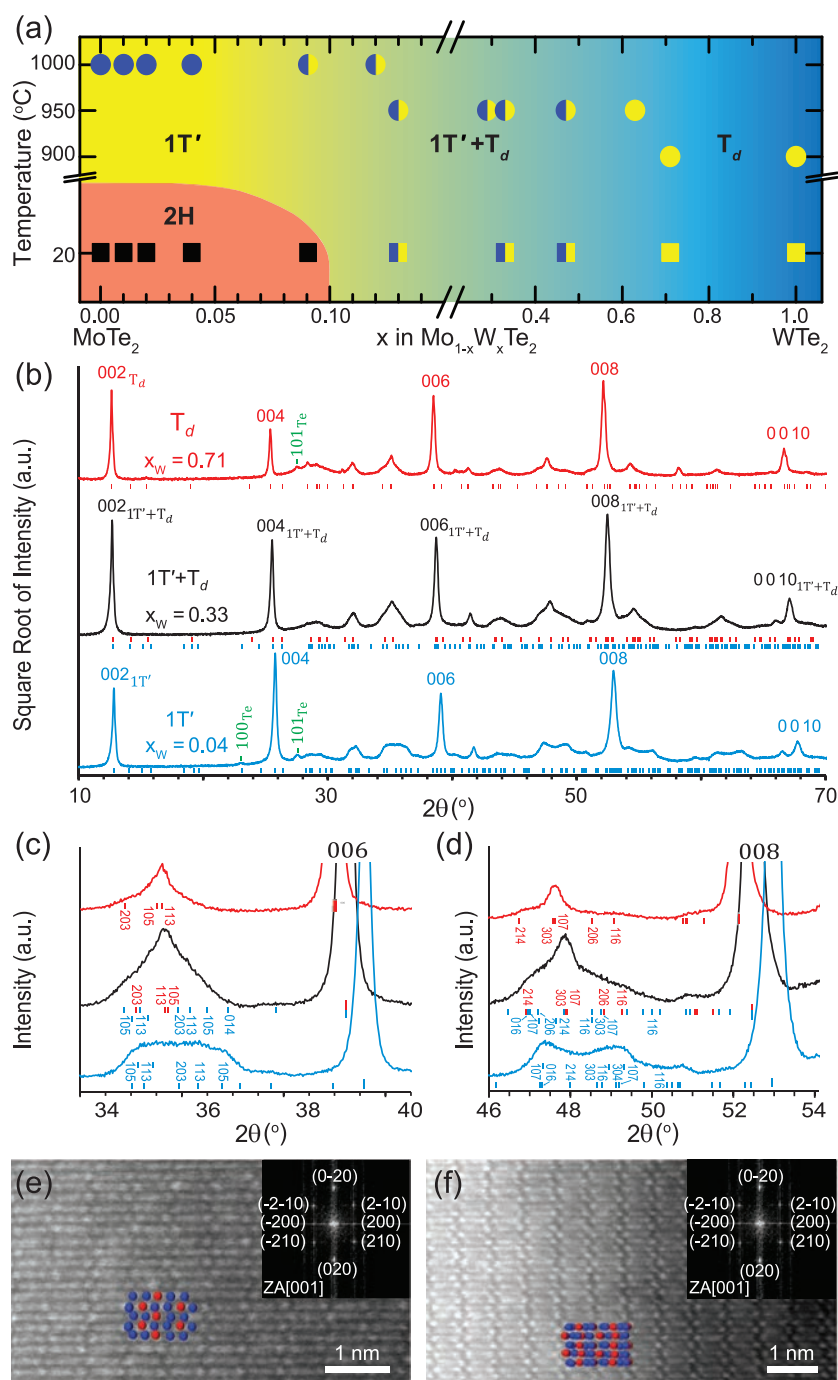


Figure 1. (a) Temperature-composition map of crystal phases in the MoTe_2 - WTe_2 system, identified from the XRD analysis. Circles correspond to the samples that were quenched from the growth temperature indicated on the y -axis (for example, 3 adjacent circles in the upper-left corner represent $\text{Mo}_{1-x}\text{W}_x\text{Te}_2$ alloys with $x = 0, 0.01$, and 0.02 that were quenched from the growth temperature of 1000°C), and squares correspond to the samples that were additionally annealed in vacuum at 750°C after growth and slowly cooled to room temperature. Blue circles correspond to $1T'$ single-phase alloys, yellow circles and squares correspond to T_d single-phase alloys, half-filled blue + yellow circles correspond to two-phase $1T' + T_d$ mixture, and black squares are single-phase $2H$ alloys. The pink area at the bottom-left schematically denotes the single-phase $2H$ region, which extends from $x = 0$ to $x = 0.09 \pm 0.01$ at room temperature. (b) XRD θ - 2θ scans of three most representative $\text{Mo}_{1-x}\text{W}_x\text{Te}_2$ samples with $x = 0.04$ (single-phase $1T'$ alloy), $x = 0.33$ (two-phase $1T' + T_d$ mixture), and $x = 0.71$ (single-phase T_d alloy). (c,d) Enlarged XRD scans near 006 and 008 reflections that compare single-phased $x = 0.04$ ($1T'$) and $x = 0.71$ (T_d) alloys with $x = 0.33$ two-phase mixture. Reflections position and $hkl(s)$ for figures 1(b) and (d) are listed in table S2 in the supporting information. (e) and (f) HAADF-STEM images of $\text{Mo}_{1-x}\text{W}_x\text{Te}_2$ samples with (e) $x = 0.04$ in $1T'$ phase and (f) $x = 0.71$ in T_d phase, together with fast fourier transforms (FFT) in the insets. Atomic models are superimposed on the images where Te atoms are blue spheres and Mo/W atoms are red spheres.

the results of the Raman tensor analysis fitting to the Raman peaks of $1T'$ - MoTe_2 and WTe_2 in figures S4, S5, and supporting note 2 of the supporting information. In table 1 we summarize the experimentally-determined mode assignments for $1T'$ - MoTe_2 and T_d - WTe_2 ,

as well as the results of our DFT calculations of the $1T'$ - MoTe_2 , T_d - MoTe_2 , and T_d - WTe_2 . In the $1T'$ phase, the A_g and B_g modes are Raman-active while the A_u and B_u modes are only infrared-active. Interestingly, all modes are Raman active for the T_d phase.

Table 1. Theoretically predicted and experimentally measured wavenumbers, ω_{calc} and ω_{exp} , respectively, alongside their associated symmetries.

| 1T'-MoTe ₂ | | | T _d -MoTe ₂ | | T _d -WTe ₂ | | |
|--|---|----------------|--|----------------|--|--|----------------|
| ω_{calc} (cm ⁻¹) | ω_{exp} (cm ⁻¹) | Symmetry | ω_{calc} (cm ⁻¹) | Symmetry | ω_{calc} (cm ⁻¹) | ω_{calc} (cm ⁻¹) | Symmetry |
| 76.81 | 78 | A _g | 76.96 | A ₁ | 79.0 | 80 | A ₁ |
| 85.56 | | A _g | 85.74 | B ₁ | 84.6 | 91 | A ₂ |
| 88.20 | | B _g | 88.09 | B ₂ | 84.7 | | B ₂ |
| 90.88 | | B _g | 90.68 | A ₂ | 86.2 | | B ₁ |
| 104.90 | 107 | B _g | 104.88 | A ₂ | 107.7 | | B ₂ |
| 105.61 | 111 | B _g | 105.52 | B ₂ | 107.7 | | B ₂ |
| 108.37 | | A _u | 108.37 | A ₂ | 110.9 | 111 | A ₂ |
| 108.67 | | A _g | 108.71 | A ₁ | 111.5 | 117 | A ₁ |
| 110.80 | | A _u | 110.76 | B ₂ | 112.6 | | B ₂ |
| 113.60 | 111 | A _g | 113.61 | B ₁ | 115.3 | | B ₁ |
| 115.38 | | B _u | 115.53 | B ₁ | 120.6 | | B ₁ |
| 123.82 | | B _u | 123.23 | A ₁ | 127.2 | 132 | A ₁ |
| 125.52 | | A _g | 126.23 | A ₁ | 127.4 | | B ₁ |
| 128.25 | 128 | A _g | 128.07 | B ₁ | 128.5 | 134 | A ₁ |
| 129.60 | | B _u | 129.92 | B ₁ | 130.4 | 137 | A ₁ |
| 134.80 | | B _u | 134.84 | A ₁ | 131.3 | | B ₁ |
| 155.54 | | A _g | 155.59 | B ₁ | 146.3 | | A ₂ |
| 159.24 | 163 | A _g | 159.35 | A ₁ | 146.6 | | A ₂ |
| 176.52 | | A _u | 176.64 | A ₂ | 152.4 | | B ₁ |
| 176.97 | | A _u | 176.87 | B ₂ | 153.7 | | A ₂ |
| 187.99 | | B _g | 188.27 | A ₂ | 155.4 | | A ₁ |
| 189.20 | 192 | B _g | 189.29 | B ₂ | 156.2 | | B ₂ |
| 192.13 | | B _u | 192.11 | B ₁ | 165.6 | | B ₁ |
| 192.33 | | B _u | 192.25 | A ₁ | 166.2 | 164 | A ₁ |
| 247.13 | | A _g | 247.24 | A ₁ | 201.2 | | A ₁ |
| 249.03 | | A _g | 248.99 | B ₁ | 201.5 | | B ₁ |
| 251.58 | 251 | A _g | 251.48 | A ₁ | 204.6 | 212 | A ₁ |
| 254.14 | 260 | A _g | 253.95 | B ₁ | 206.1 | | B ₁ |
| 265.96 | | B _u | 266.14 | B ₁ | 227.9 | | A ₁ |
| 267.37 | | B _u | 267.42 | A ₁ | 228.4 | | B ₁ |

The polarized Raman maps presented in figure S3 of the supporting information are instructional for an overview of the composition-induced evolution of the vibrational modes from the 1T' phase to the T_d phase. However, the sensitivity of the Raman spectrum to the orientation of the excitation and analyzer complicates further interpretation of the data in this form. To eliminate this orientation-dependence, we sum the parallel and perpendicular data over all angular orientations (figures 2(e) and (f)). The composition-dependent Raman spectra of the alloys show several important features. Most modes are present in all compositions and exhibit only small frequency shifts due to the similarity between the 1T' and T_d lattices (figures 2(a) and (d)). However, certain Raman modes (identified with boxes in figures 2(e) and (f)) exhibit unique behavior that is dependent on structural symmetry and composition x in the alloys.

We direct our attention first to the Raman peak observed at 128 cm⁻¹ (box i of figures 2(e) and 3(a)). For $x = 0$, this feature corresponds to an A_g symmetry mode in MoTe₂, as demonstrated by our polarization-

resolved measurements, DFT calculations [36], and other literature observations [10, 18, 48]. This mode is a single peak for compositions $x \leq 0.04$, which is consistent with the inversion symmetric 1T' phase. For compositions $x = 0.09$ and 0.12, however, the 128 cm⁻¹ mode broadens and is best fit by a pair of Lorentzian functions. Finally, for $x \geq 0.29$, the 128 cm⁻¹ mode splits into two well-resolved peaks. The separation between these two peaks is presented versus composition in figure 3(c) and illustrates the appearance and evolution of the doublet, which persists into the $x = 1$ (pure WTe₂) case but with a smaller peak separation. Temperature-dependent electrical and XRD measurements have previously shown that MoTe₂ undergoes a temperature-induced phase transition from the 1T' to T_d crystal structure when cooled below 250 K [16, 17]. Recent temperature-dependent Raman measurements in [18] have also demonstrated that the A_g mode at 128 cm⁻¹ in MoTe₂ splits into a doublet with A₁ mode symmetry due to inversion-symmetry breaking upon transitioning into the T_d phase at low temperatures. Our XRD measurements identify the $0.04 < x < 0.63$

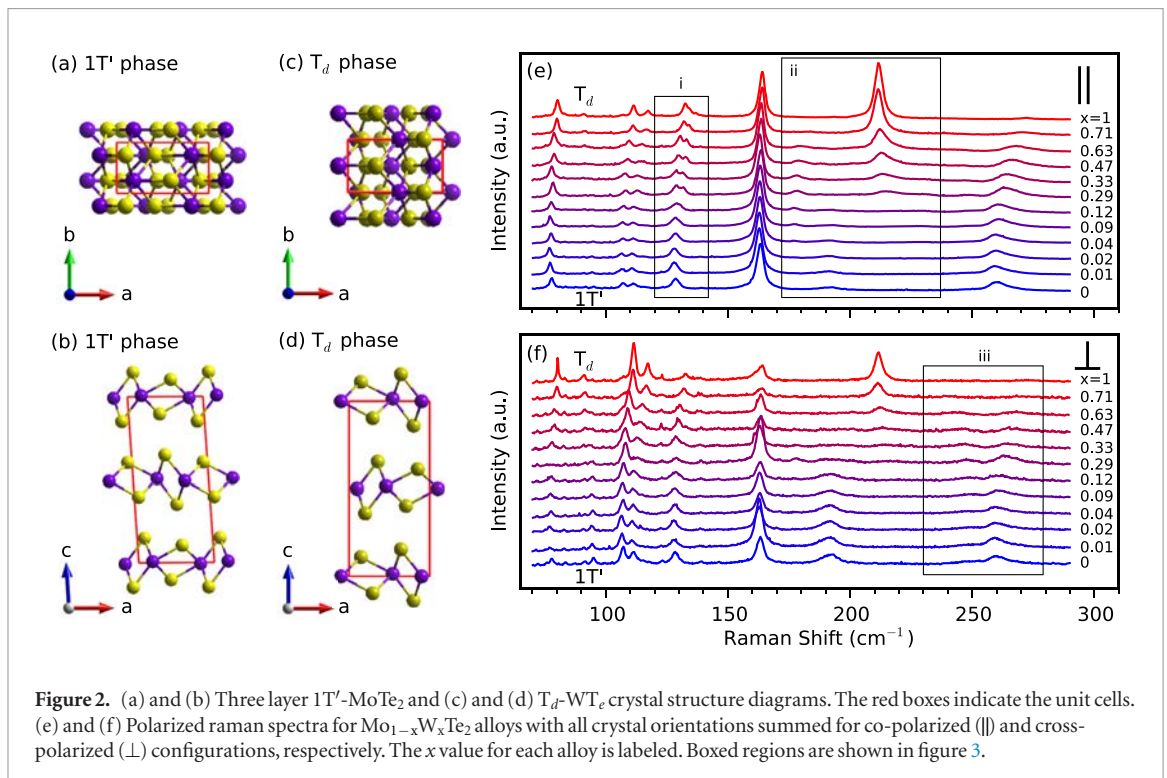


Figure 2. (a) and (b) Three layer $1T'$ - MoTe_2 and (c) and (d) T_d - WTe_2 crystal structure diagrams. The red boxes indicate the unit cells. (e) and (f) Polarized Raman spectra for $\text{Mo}_{1-x}\text{W}_x\text{Te}_2$ alloys with all crystal orientations summed for co-polarized (\parallel) and cross-polarized (\perp) configurations, respectively. The x value for each alloy is labeled. Boxed regions are shown in figure 3.

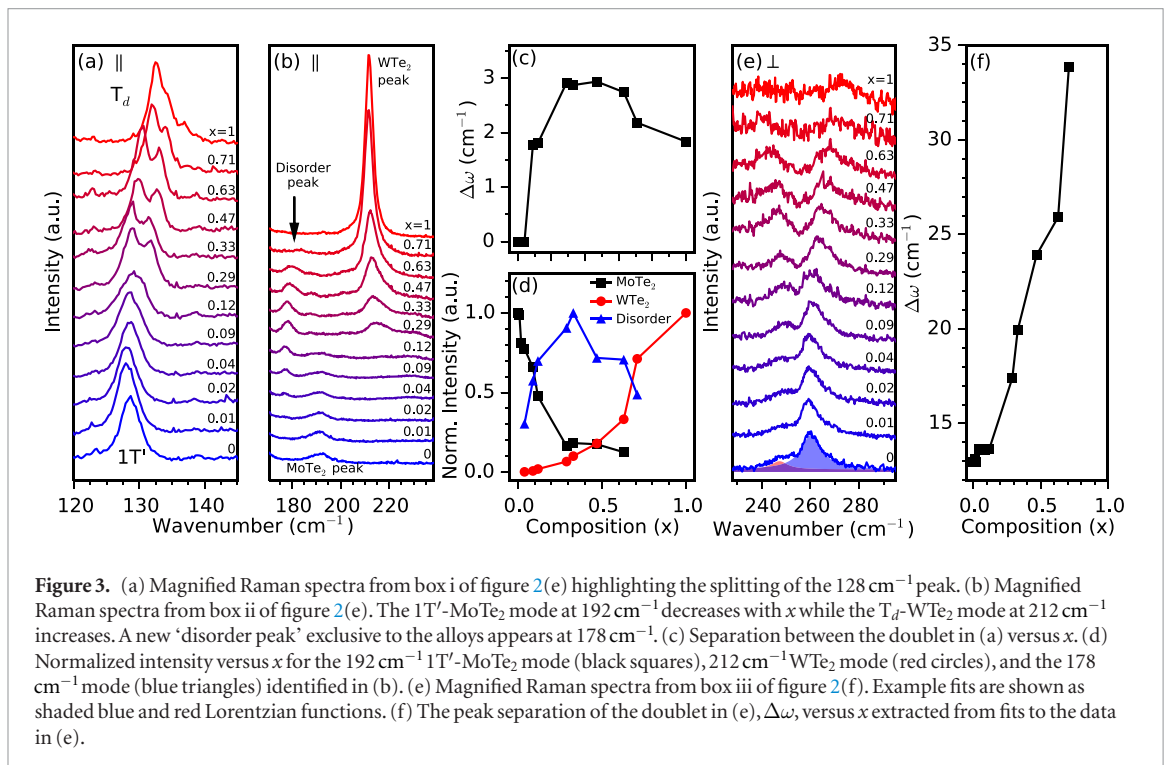


Figure 3. (a) Magnified Raman spectra from box i of figure 2(e) highlighting the splitting of the 128 cm^{-1} peak. (b) Magnified Raman spectra from box ii of figure 2(e). The $1T'$ - MoTe_2 mode at 192 cm^{-1} decreases with x while the T_d - WTe_2 mode at 212 cm^{-1} increases. A new ‘disorder peak’ exclusive to the alloys appears at 178 cm^{-1} . (c) Separation between the doublet in (a) versus x . (d) Normalized intensity versus x for the 192 cm^{-1} $1T'$ - MoTe_2 mode (black squares), 212 cm^{-1} WTe_2 mode (red circles), and the 178 cm^{-1} mode (blue triangles) identified in (b). (e) Magnified Raman spectra from box iii of figure 2(f). Example fits are shown as shaded blue and red Lorentzian functions. (f) The peak separation of the doublet in (e), $\Delta\omega$, versus x extracted from fits to the data in (e).

region as two-phase, and therefore we cannot interpret the appearance of the doublet as signifying a phase transition from $1T'$ to T_d . Instead, we attribute the doublet to the breakdown of inversion symmetry in the $1T'$ - $\text{Mo}_{1-x}\text{W}_x\text{Te}_2$ alloys, which originates not from a $1T' \rightarrow T_d$ phase transition, but instead from the random substitution of Mo atoms with W atoms. Alloying therefore provides a means of destroying inversion symmetry without eliminating the $1T'$ phase. From these observations, it is apparent that $x \geq 0.29$ W concentration is sufficient to drive a breakdown of inver-

sion symmetry and suggests that Weyl physics may be observable even in this two-phase regime [6, 19].

We find that other modes also display sensitivity to compositional disorder and the substitution of Mo for W atoms. Box ii of figure 2(e) isolates MoTe_2 and WTe_2 Raman modes that evolve with changing composition, as well as a mode at 178 cm^{-1} that is not present in pure $1T'$ - MoTe_2 or T_d - WTe_2 . We summarize the composition-dependent relative intensities for these three peaks in figure 3(d). The ‘ MoTe_2 peak’ refers to the feature at 192 cm^{-1} (black squares) that is

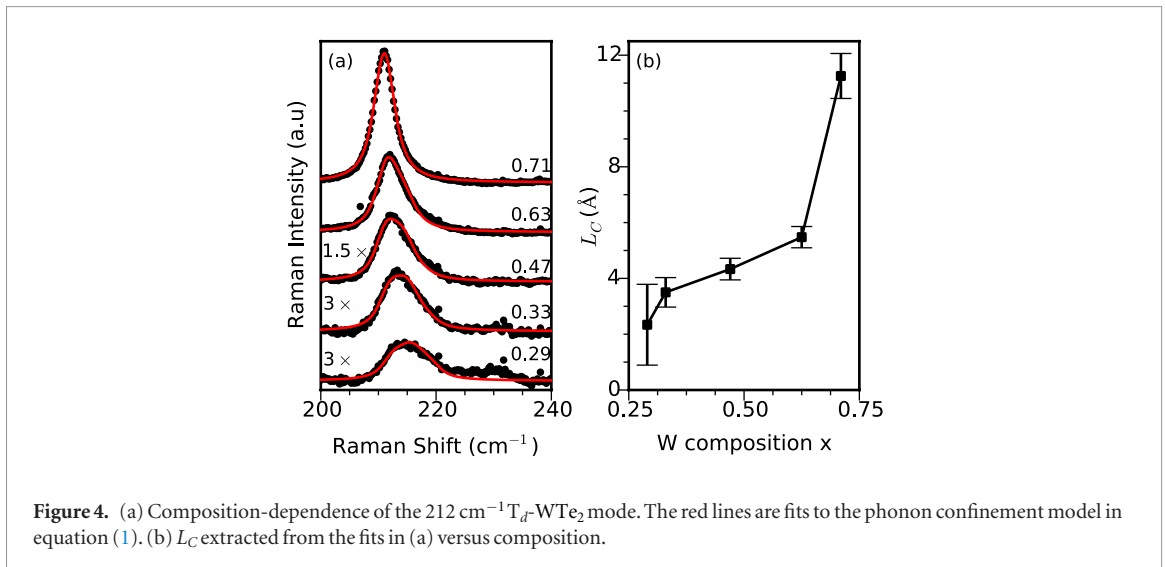


Figure 4. (a) Composition-dependence of the 212 cm⁻¹ T_d-WTe₂ mode. The red lines are fits to the phonon confinement model in equation (1). (b) L_C extracted from the fits in (a) versus composition.

present only in Mo-rich compositions (small x) and is assigned as a B_g symmetry mode in MoTe₂. The ‘WTe₂ peak’ is the large 212 cm⁻¹ feature (red circles) present only in W-rich compositions (large x) and is assigned as an A_1 symmetry mode in WTe₂. Finally, the ‘disorder peak’ refers to the 178 cm⁻¹ mode unique to the alloys. The polarization dependence of the disorder peak in the $x = 0.29$ composition can be seen in figure S6 of the supporting information. The MoTe₂ and WTe₂ peaks appear to faithfully track the removal and addition of each atomic species, while the disorder mode appears at $x = 0.02$, peaks at $x = 0.33$, and disappears at $x = 1$. The observed frequency agrees with an infrared-active, but Raman-forbidden, A_u mode at 177 cm⁻¹ predicted by our DFT calculations (table 1). We therefore suggest that the disorder mode originates from an infrared mode that is activated by the loss of translation symmetry in the lattice. The combined effects of lattice disorder and reduced Mo content at large x values drives the mode to reach its maximum intensity at $x = 0.33$, which also is the point where the ratio of the normalized intensities of the MoTe₂ peak to the WTe₂ peak approach unity. We note that similar activations of infrared modes by alloy disorder have been previously observed, particularly in Ga_xAl_{1-x}As [49].

Given the non-destructive nature and wide-spread use of Raman spectroscopy, it is desirable to determine alloy composition using a Raman-based method. The MoTe₂ Raman modes present near 260 cm⁻¹ (box iii, figure 2(f)) provide a potential measure of the alloy composition, which we demonstrate in figures 3(e) and (f). We observe a pair of broad Raman modes near 260 cm⁻¹ in MoTe₂ that are assigned as A_g modes (box iii of figures 2(f) and 3(e)) and have been seen in prior studies [36, 48]. By fitting these two peaks in each spectrum to Lorentzians, we can track the peak separation with composition. We find that the separation between these two features increases with increasing x , and that we can use it to estimate global W content in a Mo_{1-x}W_xTe₂ crystal (figure 3(f)). Our results indicate that this

method will be effective for $x > 0.09$, and is therefore most appropriate for higher W concentrations.

Finally, we examine the primary WTe₂ peak at 212 cm⁻¹ which is broad and asymmetric upon its appearance at $x = 0.29$, but sharpens as $x \rightarrow 1$ (figure 3(b)). We magnify this feature in figure 4(a) for select compositions. The asymmetric lineshape of the 212 cm⁻¹ peak provides valuable information regarding the incorporation of W into the Mo_{1-x}W_xTe₂ lattice. We find that the asymmetry of this feature and its evolution with x can be well understood in the context of the phonon confinement model, also referred to as the spatial correlation model [49, 50]. The phonon confinement model accounts for relaxation of the $\vec{q} = 0$ Raman selection rule by multiplying the Lorentzian function, used to represent standard Raman peaks in a pure crystal, with a Gaussian function of the form $\exp(-q^2L_C^2/4)$. Thus, the intensity I of Raman peaks in the phonon confinement model is given by [49]

$$I(\omega) \propto \int_{\text{BZ}} \exp\left(\frac{-q^2L_C^2}{4}\right) \frac{d^3q}{[\omega - \omega(q)]^2 + (\Gamma_0/2)^2}, \quad (1)$$

where \vec{q} is in units of $(2\pi/a, 2\pi/b, 2\pi/c)$, $a = 6.3109 \text{ \AA}$, $b = 3.5323 \text{ \AA}$, and $c = 14.4192 \text{ \AA}$ are the DFT-relaxed lattice parameters of WTe₂, $\Gamma_0 = 3.80 \text{ cm}^{-1}$ is the full width at half maximum of the W peak for composition $x = 1$, $\omega(q)$ is the dispersion relation which we calculate from DFT and shift to match the experimental value of $\omega(0)$ (figure S1 of the supporting information), and L_C is the phonon correlation length. In a pure crystal, L_C is infinite due to the translational symmetry of the lattice and results in plane wave eigenstates. The Gaussian factor in equation (1), in this case, is zero for all \vec{q} except the Γ point, and therefore the $\vec{q} = 0$ Raman selection rule is preserved. However, Mo_{1-x}W_xTe₂ alloys exhibit potential fluctuations due to the substitutional doping on the transition metal sublattice. The random positioning of the dopant atoms destroys translational symmetry in the crystal, thereby yielding a finite L_C and relaxing the $\vec{q} = 0$ Raman selection rule. We fit the

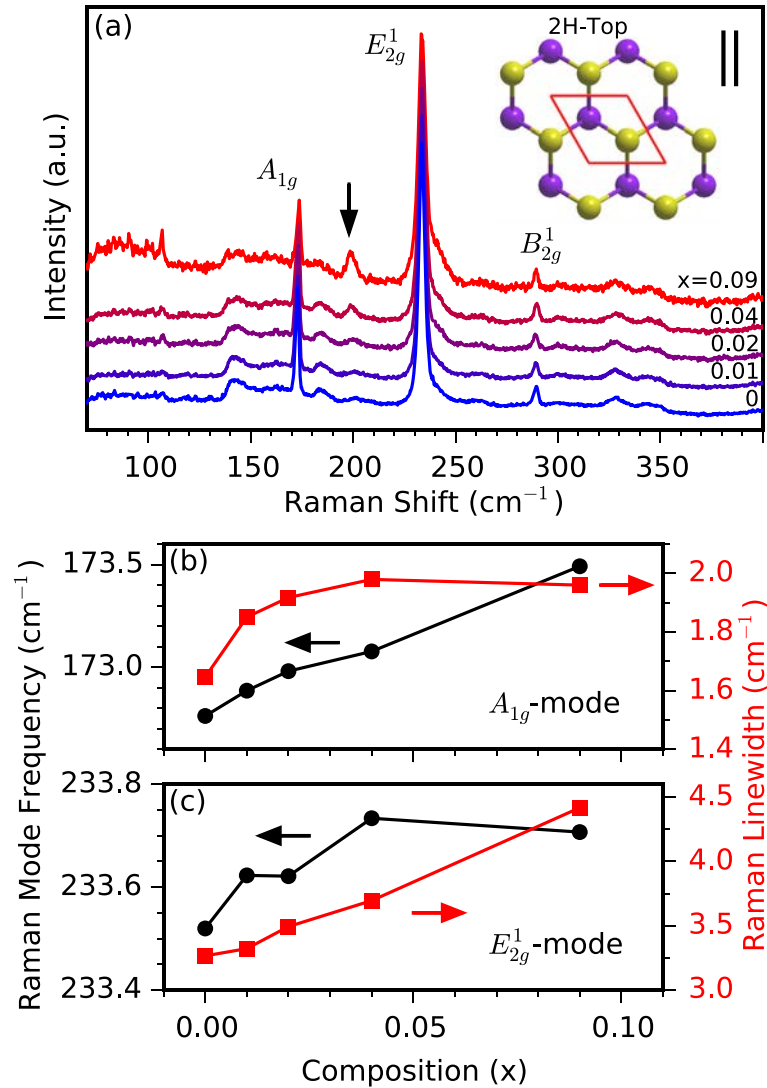


Figure 5. (a) Normalized Raman spectra of 2H-Mo_{1-x} alloys measured in the co-polarized configuration. The double-resonance Raman mode is indicated with the black arrow. Inset: crystal structure of 2H-Mo_{1-x}. (b) and (c) illustrate the evolution in frequencies (black, left axis) and linewidths (red, right axis) of the A_{1g} and E_{2g}¹ modes, respectively.

212 cm⁻¹ W peak for $x \geq 0.29$ in background-subtracted Raman spectra with this model (red lines in figure 4(a)) using experimentally-derived parameters and the DFT calculated phonon dispersion. The extracted phonon correlation length L_C is plotted versus x in figure 4(b), and is found to increase rapidly with x .

We now comment on the Raman spectra of 2H-Mo_{1-x}W_xTe₂ ($x = 0 \rightarrow 0.09$), which are shown in figure 5(a). The A_{1g} (173 cm⁻¹), E_{2g}¹ (234 cm⁻¹), and B_{2g}¹ (289 cm⁻¹) modes are visible in all compounds (figure 5(a)) and exhibit only small changes. The shifts in mode frequency and linewidth for the A_{1g} and E_{2g}¹ modes are summarized in figures 5(b) and (c). For $x = 0.09$, we find that the A_{1g} and E_{2g}¹ modes develop asymmetric tails on the low and high energy sides of the peak, respectively. This asymmetry originates from a finite phonon correlation length as discussed previously and we note that the direction of the tail for each mode is consistent with the phonon dispersions of 2H-MoTe₂

[51]. In addition, we identify a feature appearing at 202 cm⁻¹ for $0.02 \leq x \leq 0.09$ alloys which we assign as a double-resonance Raman mode originating from the scattering of two longitudinal acoustic phonons from the M-point or an E_{1g}(M) and a transverse acoustic mode, both also from the M point [38]. This feature has only been observed in few-layer 2H-MoTe₂ under resonant excitation [38], and its appearance in the bulk alloy samples is believed to originate from an enhancement in $\bar{q} \neq 0$ Raman scattering processes by compositional disorder in the lattice.

4. Conclusion

We have used XRD, STEM, DFT, and Raman spectroscopy to characterize the different crystal phases spanned by the Mo_{1-x}W_xTe₂ alloy system. XRD and STEM measurements determined that 1T'/T_d-Mo_{1-x}W_xTe₂ alloys are in the 1T' phase for $x \leq 0.04$ and the T_d phase for $x \geq 0.63$. For compositions $0.04 < x < 0.63$,

$\text{Mo}_{1-x}\text{W}_x\text{Te}_2$ exists in a $1T' + T_d$ two-phase mixture. Raman measurements enable the assignment of phonon mode symmetries across the compositional phase space and permit the observation of a new disorder-activated mode unique to $\text{Mo}_{1-x}\text{W}_x\text{Te}_2$ alloys. Furthermore, we find that inversion symmetry breaking in the $1T'$ phase can occur without transitioning to an orthorhombic configuration by monitoring the splitting of the 128cm^{-1} peak. Finally, we find that the asymmetry of the primary WTe_2 peak can be captured by the phonon confinement model, which in turn allows for the determination of the phonon correlation length. Our studies of the $2H$ phase show small changes in mode frequencies with x and provide evidence for disorder enhancement of double-resonance Raman scattering processes. These measurements are foundational for future studies seeking to explore the electronic, vibrational, or topological properties of $\text{Mo}_{1-x}\text{W}_x\text{Te}_2$ alloys.

Acknowledgments

SMO, JJ, IRS, and PMV acknowledge support from the Office of Naval Research through Grant No. N-00014-15-1-2357, the George Mason University OSCAR Program, and the George Mason University Presidential Scholarship Program. RB thanks the National Research Council Research Associateship Programs for its support. SK acknowledges support from the US Department of Commerce, National Institute of Standards and Technology under the financial assistance award 70NANB16H043. AKS is funded by the Professional Research Experience Postdoctoral Fellowship under award No. 70NANB11H012. This research used computational resources provided by the Texas Advanced Computing Center under Contract TG-DMR150006. This work used the Extreme Science and Engineering Discovery Environment (XSEDE), which was supported by National Science Foundation grant number ACI-1053575. AVD, SK, IK, and AB acknowledge the support of Material Genome Initiative funding allocated to NIST.

ORCID iDs

Sean M Oliver  <https://orcid.org/0000-0003-3848-5632>

Ryan Beams  <https://orcid.org/0000-0003-2592-6064>
Arunima K Singh  <https://orcid.org/0000-0002-7212-6310>

Jaydeep Joshi  <https://orcid.org/0000-0002-8024-0586>

Albert V Davydov  <https://orcid.org/0000-0003-4512-2311>

Patrick M Vora  <https://orcid.org/0000-0003-3967-8137>

References

- [1] Mak K F and Shan J 2016 Photonics and optoelectronics of 2D semiconductor transition metal dichalcogenides *Nat. Photon.* **10** 216–26
- [2] Qi Y *et al* 2016 Superconductivity in Weyl semimetal candidate MoTe_2 *Nat. Commun.* **7** 11038
- [3] Pan X-C *et al* 2015 Pressure-driven dome-shaped superconductivity and electronic structural evolution in tungsten ditelluride *Nat. Commun.* **6** 7805
- [4] Kang D *et al* 2015 Superconductivity emerging from a suppressed large magnetoresistant state in tungsten ditelluride *Nat. Commun.* **6** 7804
- [5] Qian X, Liu J, Fu L and Li J 2014 Quantum spin Hall effect in two-dimensional transition metal dichalcogenides *Science* **346** 1344–7
- [6] Soluyanov A A, Gresch D, Wang Z, Wu Q, Troyer M, Dai X and Bernevig B A 2015 Type-II Weyl semimetals *Nature* **527** 495–8
- [7] Xu S-Y *et al* 2015 Discovery of a Weyl fermion semimetal and topological Fermi arcs *Science* **349** 613–7
- [8] Tamai A *et al* 2016 Fermi arcs and their topological character in the candidate type-II Weyl semimetal MoTe_2 *Phys. Rev. X* **6** 031021
- [9] Geim A K and Grigorieva I V 2013 Van der Waals heterostructures *Nature* **499** 419–25
- [10] Park J C *et al* 2015 Phase-engineered synthesis of centimeter-scale $1T'$ - and $2H$ -Molybdenum ditelluride thin films *ACS Nano* **9** 6548–54
- [11] Wilson J A and Yoffe A D 1969 The transition metal dichalcogenides discussion and interpretation of the observed optical, electrical and structural properties *Adv. Phys.* **18** 193–335
- [12] Dawson W G and Bullett D W 1987 Electronic structure and crystallography of MoTe_2 and WTe_2 *J. Phys. C: Solid State Phys.* **20** 6159–74
- [13] Keum D H *et al* 2015 Bandgap opening in few-layered monoclinic MoTe_2 *Nat. Phys.* **11** 482–6
- [14] Naylor C H *et al* 2016 Monolayer single-crystal $1T'$ - MoTe_2 grown by chemical vapor deposition exhibits weak antilocalization effect *Nano Lett.* **16** 4297–304
- [15] Zhou L *et al* 2015 Large-area synthesis of high-quality uniform few-layer MoTe_2 *J. Am. Chem. Soc.* **137** 11892–5
- [16] Hughes H P and Friend R H 1978 Electrical resistivity anomaly in β - MoTe_2 (metallic behaviour) *J. Phys. C: Solid State Phys.* **11** L103–5
- [17] Clarke R, Marseglia E and Hughes H P 1978 A low-temperature structural phase transition in β - MoTe_2 *Phil. Mag.* **B 38** 121–6
- [18] Chen S-Y, Goldstein T, Venkataraman D, Ramasubramanian A and Yan J 2016 Activation of new Raman modes by inversion symmetry breaking in type II Weyl semimetal candidate T' - MoTe_2 *Nano Lett.* **16** 5852–60
- [19] Sun Y, Wu S-C, Ali M N, Felser C and Yan B 2015 Prediction of Weyl semimetal in orthorhombic MoTe_2 *Phys. Rev. B* **92** 161107
- [20] Chang T-R *et al* 2016 Prediction of an arc-tunable Weyl Fermion metallic state in $\text{Mo}_x\text{W}_{1-x}\text{Te}_2$ *Nat. Commun.* **7** 10639
- [21] Wang Z, Gresch D, Soluyanov A A, Xie W, Kushwaha S, Dai X, Troyer M, Cava R J and Bernevig B A 2016 MoTe_2 : a type-II Weyl topological metal *Phys. Rev. Lett.* **117** 056805
- [22] Huang L *et al* 2016 Spectroscopic evidence for a type II Weyl semimetallic state in MoTe_2 *Nat. Mater.* **15** 1155–60
- [23] Deng K *et al* 2016 Experimental observation of topological Fermi arcs in type-II Weyl semimetal MoTe_2 *Nat. Phys.* **12** 1105–10
- [24] Duerloo K-A N, Li Y and Reed E J 2014 Structural phase transitions in two-dimensional Mo- and W-dichalcogenide monolayers *Nat. Commun.* **5** 4214

- [25] Duerloo K-A N and Reed E J 2016 Structural phase transitions by design in monolayer alloys *ACS Nano* **10** 289–97
- [26] Li Y, Duerloo K-A N, Wauson K and Reed E J 2016 Structural semiconductor-to-semimetal phase transition in two-dimensional materials induced by electrostatic gating *Nat. Commun.* **7** 10671
- [27] Zhang C *et al* 2016 Charge mediated reversible metal-insulator transition in monolayer MoTe₂ and W_xMo_{1-x}Te₂ alloy *ACS Nano* **10** 7370–5
- [28] Huang H H, Fan X, Singh D J, Chen H, Jiang Q and Zheng W T 2016 Controlling phase transition for single-layer MTe₂ (M = Mo and W): modulation of the potential barrier under strain *Phys. Chem. Chem. Phys.* **18** 4086–94
- [29] Belopolski I *et al* 2016 Fermi arc electronic structure and chern numbers in the type-II Weyl semimetal candidate Mo_xW_{1-x}Te₂ *Phys. Rev. B* **94** 085127
- [30] Revolinsky E and Beerntsen D 1964 Electrical properties of the MoTe₂-WTe₂ and MoSe₂-WSe₂ systems *J. Appl. Phys.* **35** 2086–9
- [31] Champion J A 1965 Some properties of (Mo, W) (Se, Te)₂ *Br. J. Appl. Phys.* **16** 1035–7
- [32] Rhodes D *et al* 2017 Engineering the structural and electronic phases of MoTe₂ through W substitution *Nano Lett.* **17** 1616–22
- [33] Lv Y-Y *et al* 2017 Composition and temperature-dependent phase transition in miscible Mo_{1-x}W_xTe₂ single crystals *Sci. Rep.* **7** 44587
- [34] Yan X-J *et al* 2017 Composition dependent phase transition and its induced hysteretic effect in the thermal conductivity of W_xMo_{1-x}Te₂ *Appl. Phys. Lett.* **110** 211904
- [35] Liu W L *et al* 2016 Effect of aging-induced disorder on the quantum transport properties of few-layer WTe₂ *2D Mater.* **4** 011011
- [36] Beams R *et al* 2016 Characterization of few-layer 1T' MoTe₂ by polarization-resolved second harmonic generation and raman scattering *ACS Nano* **10** 9626–36
- [37] Ribeiro H B *et al* 2015 Unusual angular dependence of the raman response in black phosphorus *ACS Nano* **9** 4270–6
- [38] Guo H *et al* 2015 Double resonance Raman modes in monolayer and few-layer MoTe₂ *Phys. Rev. B* **91** 205415
- [39] Kresse G and Furthmüller J 1996 Efficient iterative schemes for *ab initio* total-energy calculations using a plane-wave basis set *Phys. Rev. B* **54** 11169–86
- [40] Klimeš J, Bowler D R and Michaelides A 2011 Van der Waals density functionals applied to solids *Phys. Rev. B* **83** 195131
- [41] Togo A and Tanaka I 2015 First principles phonon calculations in materials science *Scr. Mater.* **108** 1–5
- [42] Aroyo M I, Kirov A, Capillas C, Perez-Mato J M and Wondratschek H 2006 Bilbao crystallographic server II representations of crystallographic point groups and space groups *Acta Crystallogr. A* **62** 115–28
- [43] Revolinsky E and Beerntsen D J 1966 Electrical properties of α - and β -MoTe₂ as affected by stoichiometry and preparation temperature *J. Phys. Chem. Solids* **27** 523–6
- [44] Sakai H, Ikeura K, Bahramy M S, Ogawa N, Hashizume D, Fujioka J, Tokura Y and Ishiwata S 2016 Critical enhancement of thermopower in a chemically tuned polar semimetal MoTe₂ *Sci. Adv.* **2** e1601378
- [45] Zhou L *et al* 2017 A sensitive phonon-based probe for structure identification of 1T' MoTe₂ *J. Am. Chem. Soc.* **139** 8396–9
- [46] Jiang Y C, Gao J and Wang L 2016 Raman fingerprint for semi-metal WTe₂ evolving from bulk to monolayer *Sci. Rep.* **6** 19624
- [47] Song Q *et al* 2016 The in-plane anisotropy of WTe₂ investigated by angle-dependent and polarized raman spectroscopy *Sci. Rep.* **6** 29254
- [48] Ma X *et al* 2016 Raman scattering in the transition-metal dichalcogenides of 1T'-MoTe₂, T_d-MoTe₂, and T_d-WTe₂ *Phys. Rev. B* **94** 214105
- [49] Parayanthal P and Pollak F H 1984 Raman scattering in alloy semiconductors: 'spatial correlation' model *Phys. Rev. Lett.* **52** 1822–5
- [50] Mignuzzi S *et al* 2015 Effect of disorder on Raman scattering of single-layer MoS₂ *Phys. Rev. B* **91** 195411
- [51] Goldstein T, Chen S-Y, Xiao D, Ramasubramanian A and Yan J 2016 Raman scattering and anomalous Stokes anti-stokes ratio in MoTe₂ atomic layers *Sci. Rep.* **6** 28024

Supporting Information: The Structural Phases and Vibrational Properties of $\text{Mo}_{1-x}\text{W}_x\text{Te}_2$ Alloys

Sean M. Oliver^{1,*}, Ryan Beams^{2,*}, Sergiy Krylyuk^{2,3}, Irina Kalish², Arunima K. Singh², Alina Bruma², Francesca Tavazza², Jaydeep Joshi¹, Iris R. Stone¹, Stephan J. Stranick², Albert V. Davydov², Patrick M. Vora^{1,†}

¹Department of Physics and Astronomy, George Mason University, Fairfax, VA 22030 USA

²Material Measurement Laboratory, National Institute of Standards and Technology, Gaithersburg, MD 20899, USA

³Theiss Research, La Jolla, CA 92037, USA

*These authors contributed equally to the work.

†Author to whom correspondence should be addressed, pvora@gmu.edu.

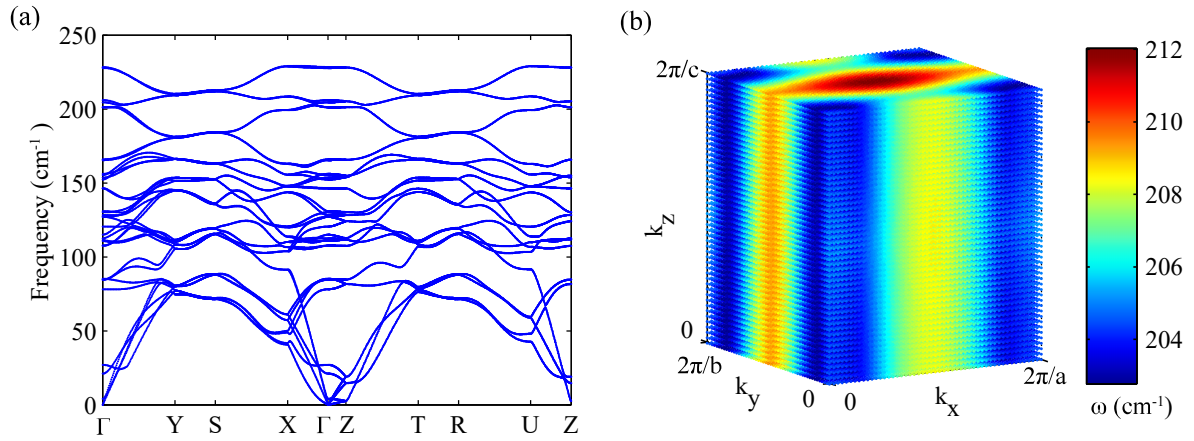


Figure S1. (a) Phonon dispersion of $T_d\text{-WTe}_2$ along high-symmetry k -paths. (b) The symbol colors denote the frequency of DFT simulated mode corresponding to the experimentally measured 212 cm^{-1} mode, on a uniform k -points mesh of $51 \times 51 \times 51$ in the irreducible orthorhombic Brillouin zone of $T_d\text{-WTe}_2$.

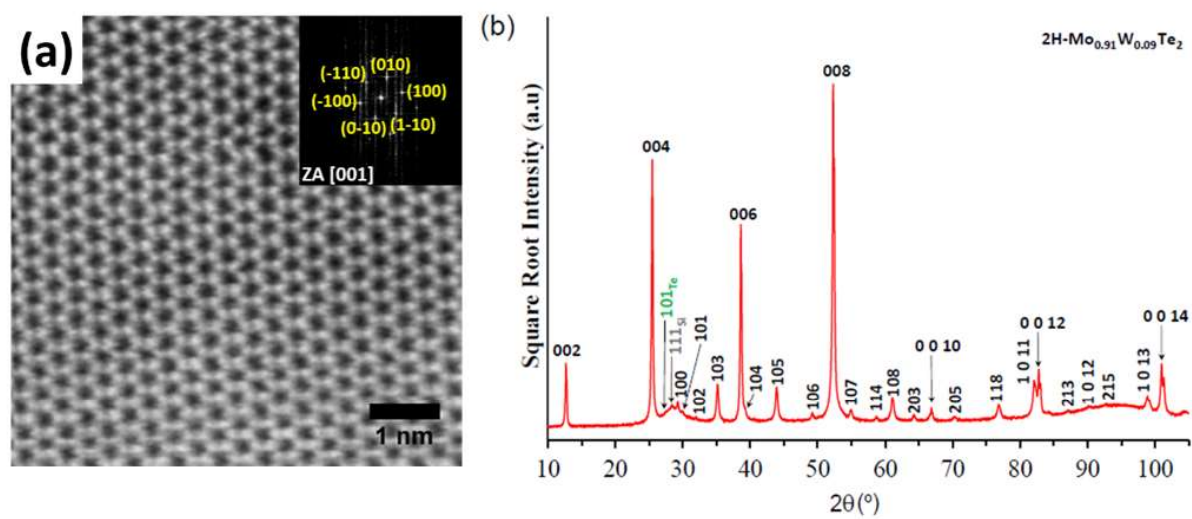


Figure S2. (a) HAADF-STEM image with FFT in the inset and (b) powder XRD scan of 2H-Mo_{0.91}W_{0.09}Te₂ alloy converted from 1T'-Mo_{0.91}W_{0.09}Te₂ crystals by thermal annealing at 750 °C for 72 hours followed by slow cooling to room temperature.

Table S1. Experimental 2θ values for $1T'$ and T_d phases for the $\text{Mo}_{1-x}\text{W}_x\text{Te}_2$ alloys with different compositions x . Corresponding lattice parameters are calculated with MDI Jade 6.5 software (Materials Data Inc., Livermore, CA 2015) using PDF #01-071-1256 (ICDD, 2012) for T_d ($\text{Pmn}2_1$) phase and PDF #01-071-2157 (ICDD, 2012) for $1T'$ ($\text{P}2_1/\text{m}$) phase as the basis of refinement. Notes: a.) $00l$ reflections in the first column ($hkl_{1T'}$) and the last column (hkl_{T_d}) are signified by the bold font; b.) 2θ values in blue font for the two-phase, $1T' + T_d$, mixture at $x=0.33$ indicate that the corresponding hkl reflections were assigned to both phases, $1T'$ and T_d .

| | x = 0 | x = 0.04 | x = 0.33 | | x = 0.71 | x = 1 | |
|-------------|--|---|---|--|---|---|-------------|
| | $1T'$ | $1T'$ | $1T'$ | T_d | T_d | T_d | |
| | a=6.338(7) Å b=3.4723(3) Å c=13.847(1) Å $\beta=94.13(7)^\circ$ | a=6.333(6) Å b=3.476(2) Å c=13.852(1) Å $\beta=93.75(5)^\circ$ | a=6.289(9) Å b=3.488(3) Å c=13.967(2) Å $\beta=93.46(8)^\circ$ | a=6.240(4) Å b=3.496(5) Å c=13.941(2) Å $\beta=90.00^\circ$ | a=6.2794(8) Å b=3.4874(9) Å c=14.0225(4) Å $\beta=90.00^\circ$ | a=6.33(2) Å b=3.53(3) Å c=14.14(1) Å $\beta=90.00^\circ$ | |
| $hkl_{1T'}$ | $2\theta_{\text{obs}} (^\circ)$ | $2\theta_{\text{obs}} (^\circ)$ | $2\theta_{\text{obs}} (^\circ)$ | $2\theta_{\text{obs}} (^\circ)$ | $2\theta_{\text{obs}} (^\circ)$ | $2\theta_{\text{obs}} (^\circ)$ | hkl_{T_d} |
| 002 | 12.80 | 12.80 | 12.66 | 12.66 | 12.62 | 12.28 | 002 |
| 004 | 25.76 | 25.76 | 25.52 | 25.52 | 25.38 | 24.96 | 004 |
| 201 | 29.39 | 29.39 | 29.52 | 35.12 | 35.11 | 34.58 | 113 |
| 013 | 32.24 | 32.24 | 32.06 | --- | --- | --- | --- |
| 006 | 39.08 | 39.08 | 38.70 | 38.70 | 38.48 | 38.02 | 006 |
| 015 | 41.70 | 41.70 | 41.44 | 41.44 | 41.28 | 40.88 | 015 |
| --- | --- | --- | --- | 47.88 | 47.5 | 47.14 | 303 |
| 008 | 52.98 | 52.94 | 52.46 | 52.46 | 52.14 | 51.62 | 008 |
| -108 | 53.98 | 54.06 | 53.68 | --- | --- | --- | --- |
| 019 | 66.58 | 66.52 | 65.91 | 65.91 | 65.57 | 65.09 | 019 |
| 0010 | 67.76 | 67.74 | 67.10 | 67.10 | 66.64 | 66.08 | 0010 |

Table S2. Calculated $1T'$ and T_d peak positions for $\text{Mo}_{1-x}\text{W}_x\text{Te}_2$ alloys with $x = 0.04, 0.33,$ and 0.71 . The 2θ values were calculated using *j*POWD 5.0 pattern and structure simulation software by Materials Data Inc., Livermore, CA, 2015, with lattice parameters from Table S1 and unit cell atom coordinates from Ref. [1]. Notes: a.) $00l$ reflections are signified by the bold font; b.) for the $1T'$ phase, reflections for $56.27^\circ < 2\theta < 67.73^\circ$ are omitted to avoid data overcrowding in the table.

| x = 0.04 | | | | x = 0.33 | | | | | | | | x = 0.71 | | | |
|-----------------|------------|----------------|-------------|-----------------|------------|----------------|-------------|----------------------|------------|----------------|-------------|----------------------|------------|----------------|-------------|
| 1T' | | | | 1T' | | | | T_d | | | | T_d | | | |
| 2 θ (°) | hkl | 2 θ (°) | hkl | 2 θ (°) | hkl | 2 θ (°) | hkl | 2 θ (°) | hkl | 2 θ (°) | hkl | 2 θ (°) | hkl | 2 θ (°) | hkl |
| 6.39 | 001 | 42.97 | -301 | 6.33 | 001 | 43.29 | -115 | 12.69 | 002 | 54.99 | 313 | 12.61 | 002 | 54.67 | 305 |
| 12.80 | 002 | 43.47 | -115 | 12.69 | 002 | 43.30 | -301 | 14.18 | 100 | 55.02 | 117 | 14.09 | 100 | 54.74 | 313 |
| 14.00 | 100 | 43.86 | 301 | 14.10 | 100 | 44.11 | 301 | 15.55 | 101 | 55.04 | 305 | 15.45 | 101 | 54.79 | 117 |
| 15.02 | -101 | 44.08 | -302 | 15.11 | -101 | 44.17 | 213 | 19.07 | 102 | 55.86 | 216 | 18.96 | 102 | 55.00 | 121 |
| 15.78 | 101 | 44.24 | 213 | 15.82 | 101 | 44.41 | -302 | 23.85 | 103 | 56.17 | 122 | 23.71 | 103 | 55.61 | 216 |
| 18.38 | -102 | 44.92 | 205 | 18.42 | -102 | 44.64 | 115 | 25.54 | 004 | 57.93 | 314 | 25.39 | 004 | 56.26 | 122 |
| 19.25 | 003 | 44.93 | 115 | 19.08 | 003 | 44.72 | 205 | 26.26 | 011 | 58.25 | 123 | 26.31 | 011 | 57.66 | 314 |
| 19.63 | 102 | 45.75 | -214 | 19.58 | 102 | 45.51 | 007 | 28.59 | 200 | 59.07 | 024 | 28.40 | 200 | 58.31 | 123 |
| 23.12 | -103 | 45.81 | 302 | 23.10 | -103 | 45.78 | -214 | 29.26 | 110 | 59.18 | 400 | 29.12 | 201 | 58.77 | 400 |
| 24.62 | 103 | 45.92 | 007 | 24.49 | 103 | 45.99 | -302 | 29.31 | 201 | 59.58 | 401 | 29.15 | 104 | 59.13 | 024 |
| 25.76 | 004 | 46.16 | -303 | 25.54 | 004 | 46.47 | -303 | 29.33 | 104 | 59.61 | 220 | 29.27 | 110 | 59.17 | 401 |
| 26.42 | 011 | 47.24 | -206 | 26.32 | 011 | 46.95 | 016 | 29.97 | 111 | 59.07 | 024 | 29.97 | 111 | 59.21 | 306 |
| 28.22 | 200 | 47.28 | -107 | 28.41 | 200 | 46.99 | -107 | 31.39 | 202 | 59.18 | 400 | 31.19 | 202 | 60.37 | 402 |
| 28.54 | -201 | 47.30 | 016 | 28.51 | -104 | 47.20 | -206 | 32.00 | 112 | 59.58 | 401 | 31.98 | 112 | 60.44 | 208 |
| 28.60 | -104 | 47.98 | 214 | 28.59 | 012 | 47.84 | 214 | 32.01 | 113 | 59.61 | 220 | 31.99 | 013 | 60.70 | 220 |
| 28.72 | 012 | 48.65 | 303 | 28.75 | -201 | 48.52 | -116 | 34.60 | 203 | 60.68 | 220 | 34.38 | 203 | 60.90 | 217 |
| 29.30 | 110 | 48.77 | -116 | 29.27 | 110 | 48.75 | 303 | 35.17 | 113 | 60.79 | 402 | 35.01 | 105 | 60.92 | 118 |
| 29.38 | 201 | 49.12 | -304 | 29.52 | 201 | 48.76 | 107 | 35.23 | 105 | 60.83 | 208 | 35.11 | 113 | 61.10 | 221 |
| 29.81 | -111 | 49.19 | 107 | 29.79 | -111 | 49.39 | -304 | 38.65 | 210 | 61.08 | 221 | 38.46 | 204 | 61.11 | 124 |
| 30.22 | 111 | 49.80 | -215 | 30.04 | 104 | 49.78 | -215 | 38.70 | 204 | 61.09 | 124 | 38.49 | 006 | 61.24 | 109 |
| 30.25 | 104 | 50.37 | 116 | 30.16 | 111 | 50.00 | 116 | 38.72 | 006 | 61.20 | 217 | 38.55 | 210 | 61.27 | 315 |
| 30.30 | -202 | 50.49 | 206 | 30.49 | -202 | 50.20 | 206 | 39.20 | 211 | 61.21 | 118 | 39.10 | 211 | 62.28 | 222 |
| 31.70 | -112 | 50.63 | 310 | 31.66 | -112 | 50.84 | 310 | 39.22 | 114 | 61.58 | 315 | 39.12 | 114 | 62.34 | 403 |
| 31.88 | 202 | 50.69 | -311 | 31.94 | 202 | 50.93 | -311 | 40.84 | 212 | 61.64 | 109 | 40.72 | 212 | 64.21 | 223 |
| 32.23 | 013 | 51.48 | 311 | 32.06 | 013 | 51.65 | 311 | 41.39 | 015 | 62.27 | 222 | 41.18 | 106 | 64.31 | 307 |
| 32.36 | 005 | 51.67 | -312 | 32.07 | 005 | 51.91 | 312 | 41.43 | 106 | 62.78 | 403 | 41.27 | 015 | 64.61 | 125 |
| 32.47 | 112 | 52.28 | 304 | 32.37 | 112 | 52.19 | 215 | 43.44 | 213 | 64.23 | 223 | 43.19 | 300 | 65.04 | 404 |
| 33.29 | -203 | 52.42 | 215 | 33.44 | -203 | 52.29 | 304 | 43.47 | 300 | 64.63 | 125 | 43.22 | 205 | 65.11 | 410 |
| 34.52 | -105 | 52.62 | 020 | 34.37 | -105 | 52.42 | 020 | 43.49 | 205 | 64.75 | 307 | 43.30 | 213 | 65.49 | 411 |
| 34.76 | -113 | 52.85 | -305 | 34.68 | -113 | 52.46 | 008 | 43.96 | 115 | 65.46 | 410 | 43.69 | 301 | 65.52 | 316 |
| 35.45 | 203 | 52.95 | 008 | 35.43 | 203 | 52.86 | 021 | 43.98 | 301 | 65.50 | 404 | 43.82 | 115 | 65.57 | 019 |
| 35.82 | 113 | 53.01 | -207 | 35.66 | 113 | 52.89 | -207 | 45.47 | 302 | 65.85 | 411 | 45.17 | 302 | 66.62 | 412 |
| 36.28 | 105 | 53.06 | 021 | 35.99 | 105 | 52.89 | 017 | 46.90 | 214 | 65.87 | 316 | 46.73 | 214 | 66.64 | 0010 |
| 36.64 | 114 | 53.21 | 312 | 36.41 | 014 | 53.07 | -305 | 47.87 | 303 | 65.90 | 019 | 47.56 | 303 | 66.68 | 218 |
| 37.25 | -204 | 53.31 | 017 | 37.35 | -204 | 53.33 | 312 | 47.91 | 107 | 66.92 | 224 | 47.61 | 107 | 66.87 | 224 |
| 38.47 | 210 | 53.53 | -313 | 38.55 | 210 | 53.68 | -108 | 48.83 | 206 | 66.93 | 026 | 48.52 | 206 | 66.89 | 026 |
| 38.71 | -211 | 54.06 | -108 | 38.63 | -114 | 53.76 | -313 | 49.26 | 116 | 66.99 | 412 | 49.07 | 116 | 67.00 | 209 |
| 38.76 | -114 | 54.39 | 022 | 38.72 | 006 | 54.17 | 022 | 51.05 | 310 | 67.03 | 218 | 50.76 | 304 | 67.45 | 119 |
| 39.07 | 006 | 54.50 | -216 | 38.81 | -211 | 54.22 | -117 | 51.07 | 215 | 67.08 | 0010 | 50.83 | 310 | 68.43 | 405 |
| 39.36 | 211 | 54.54 | -117 | 39.41 | 211 | 54.42 | -216 | 51.10 | 304 | 67.45 | 209 | 50.86 | 215 | 68.49 | 413 |
| 39.87 | 204 | 54.73 | 120 | 39.76 | 204 | 54.57 | 120 | 51.50 | 311 | 67.80 | 119 | 51.28 | 311 | 68.51 | 1010 |
| 40.04 | 114 | 55.04 | -121 | 39.81 | 114 | 54.88 | -121 | 52.29 | 020 | 68.82 | 126 | 52.14 | 008 | 68.75 | 126 |
| 40.08 | -212 | 55.29 | 121 | 40.17 | -212 | 55.11 | 121 | 52.47 | 008 | 68.88 | 413 | 52.14 | 008 | | |
| 40.77 | -106 | 55.77 | 313 | 40.54 | -106 | 55.52 | 108 | 52.83 | 312 | 68.92 | 405 | 52.43 | 020 | | |
| 41.32 | 212 | 56.04 | 108 | 41.32 | 212 | 55.82 | 313 | 52.86 | 017 | 68.96 | 1010 | 52.60 | 312 | | |
| 41.71 | 015 | 56.20 | -314 | 41.42 | 015 | 55.82 | 117 | 54.04 | 022 | | | 52.65 | 017 | | |
| 41.96 | -205 | 56.21 | -122 | 41.99 | -205 | 56.04 | -122 | 54.47 | 120 | | | 54.16 | 022 | | |
| 42.46 | -213 | 56.27 | 117 | 42.24 | 106 | 56.12 | 207 | 54.63 | 207 | | | 54.27 | 207 | | |
| 42.61 | 106 | --- | --- | 42.53 | -213 | --- | --- | 54.64 | 108 | | | 54.29 | 108 | | |
| 42.90 | 300 | 67.73 | 0010 | 43.20 | 300 | 67.08 | 0010 | 54.90 | 121 | | | 54.58 | 120 | | |

1. Supporting Note 1

1.1. Supplemental notes for Tables S1 and S2 on the XRD phase identification and lattice parameters refinement for 1T' and T_d phases in the Mo_{1-x}W_xTe₂ alloys.

a) Table S1 summarizes experimental 2θ angles with assigned hkl indices of 1T' and T_d phases with computationally refined lattice parameters using examples of Mo_{1-x}W_xTe₂ alloys with $x = 0$ (pure MoTe₂ 1T' phase), $x = 1$ (pure WTe₂ T_d phase), and intermediate $x = 0.04, 0.33,$ and 0.71 compositions.

b) Table S2 presents a complete set of computed 2θ and hkl values for the above intermediate compositions ($x = 0.04, 0.33,$ and 0.71) using the refined lattice parameters from Table S1.

c) In figure 1(b) (main text), the calculated peak positions from Table S2 are marked with the color-coded ticks (blue for 1T' and red for T_d) under each experimental XRD scan.

1.2. The detailed protocol of identifying 1T' and T_d phases in the Mo_{1-x}W_xTe₂ alloys in figure 1(b-d) of the main text.

a) First, we started with the pure 1T' MoTe₂ phase (scan is not shown in figure 1(b), but selected experimental peaks are listed in the left column of Table S1): hkl indices from the corresponding PDF #01-071-2157 ICDD file were manually assigned to experimental peaks and the set of lattice parameters were refined as shown in Table S1 under the green 1T' bar ($\alpha, \beta,$ and γ).

b) Similarly, the peak assignment and refined lattice parameters were computed for pure WTe₂ T_d phase (last column in Table S1) using the PDF #01-071-1256 ICDD file.

c) The process from a) was repeated for the $x = 0.04$ scan with all the peaks being identified as 1T' phase and no peaks left to be assigned to the T_d phase. Consequently, the refined lattice parameters for the 1T' single-phase alloy with $x = 0.04$ are listed in the second column of Table S1, and the calculated 2θ with corresponding hkl values are listed in Table S2 (first column under the “ $x = 0.04$ ” label). Notably, the lattice parameters in the $x = 0.04$ alloy have changed due to Mo being substituted for W as compared to pure 1T'-MoTe₂.

d) Similar to the process in c), all the peaks in the $x = 0.71$ alloy were identified and the lattice parameters were refined using only the T_d phase. The lattice parameters for this single-phase T_d alloy with $x = 0.71$ have changed compared to those for the pure T_d-WTe₂ compound due to Mo alloying in the WTe₂ matrix.

e) Finally, for the case of the $x = 0.33$ sample, the peaks that only belong to the 1T' phase were identified first. For example, as illustrated in figure 1(c), 1T' (-105) and (105) reflections at $\sim 34.4^\circ$ and $\sim 36.0^\circ$, respectively, cannot be assigned to the T_d phase

(notably, the (105) T_d reflection is located at $\sim 35.2^\circ$, right between these two $1T'$ peaks). Similarly, figure 1(d) shows unambiguous assignment for the (-107) and (107) $1T'$ peaks, located at $\sim 47.0^\circ$ and $\sim 48.8^\circ$, respectively, with the (107) peak of T_d phase sitting at $\sim 47.9^\circ$, right between the two $1T'$ “shoulders.”

Note: The figure 1 caption highlights that these two 2θ angle ranges, from $34-37^\circ$ (figure 1(c)) and from $48-50^\circ$ (figure 1(d)), illustrate the most prominent difference between the $1T'$ peak shapes (see lower, blue-colored scans for $1T'$ single-phase alloy with $x = 0.04$) and the T_d peak shapes (see upper, red-colored scans for T_d single-phase alloy with $x = 0.71$). Ultimately, the intermediate $x = 0.33$ alloy scan (see black-colored segments in figure 1(c) and 1(d)) can be produced by combining the blue ($1T'$) and red (T_d) components. As mentioned in “Section 3: Results and Discussion” of the main manuscript, an analogous process of using (-10l) and (10l) $1T'$ doublet peaks was used in refs. [17] and [44] to distinguish between $1T'$ and T_d phases for similar TMD systems.

After unambiguous $1T'$ peak assignments, the lattice parameters for the $1T'$ component in the $x = 0.33$ alloy were refined (as listed in column #3 under the green $1T'$ bar in Table S1). Then, the process was repeated for the remaining “non- $1T'$ ” reflections by assigning them to the T_d phase. Finally, the refined lattice parameters for $1T'$ and T_d phases in $x = 0.33$ alloy were used to compute hkl peaks in Table S2.

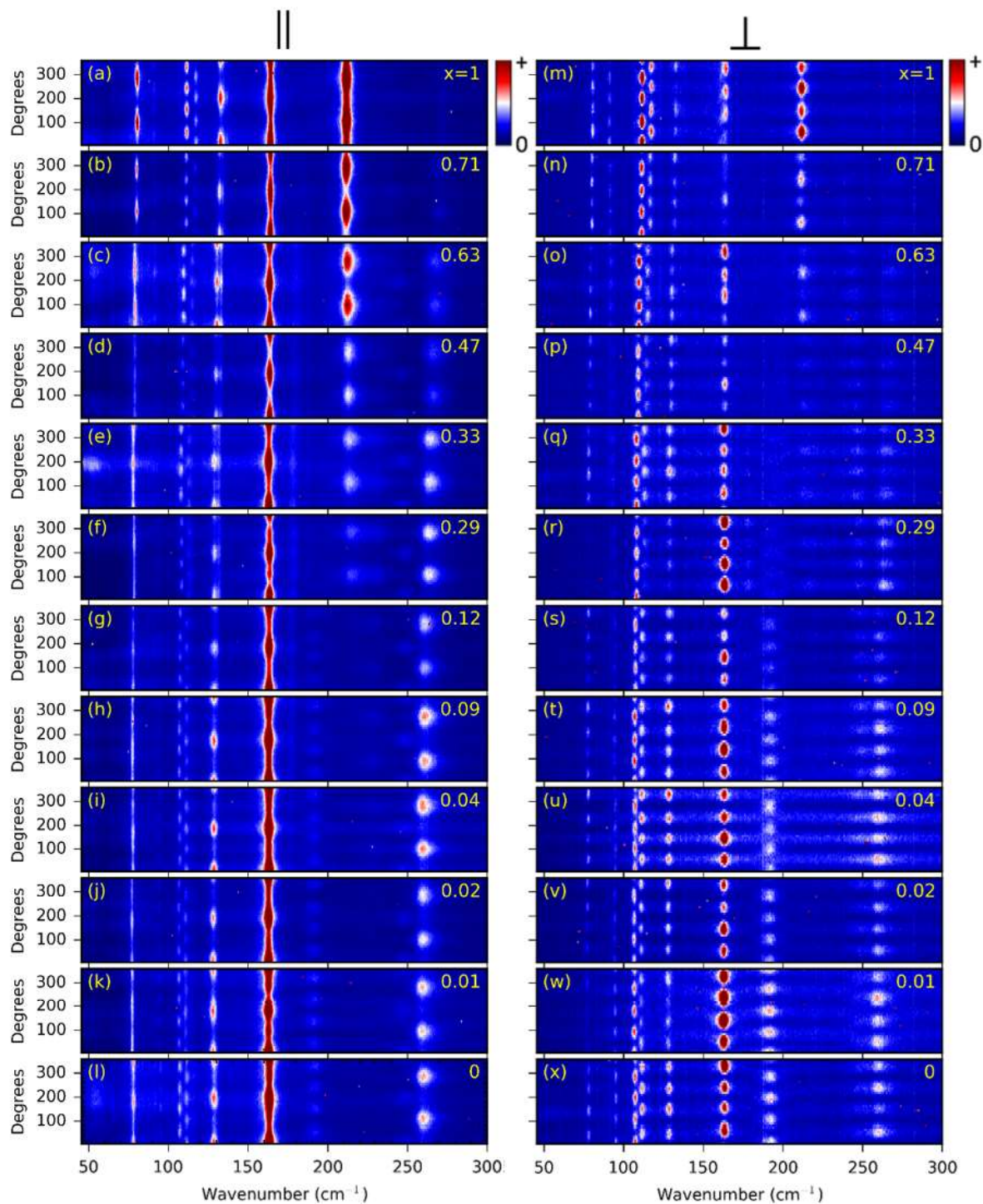


Figure S3. Polarization-dependent Raman measurements of the $\text{Mo}_{1-x}\text{W}_x\text{Te}_2$ alloys in the (a-l) co-polarized (\parallel) and (m-x) cross-polarized (\perp) configurations.

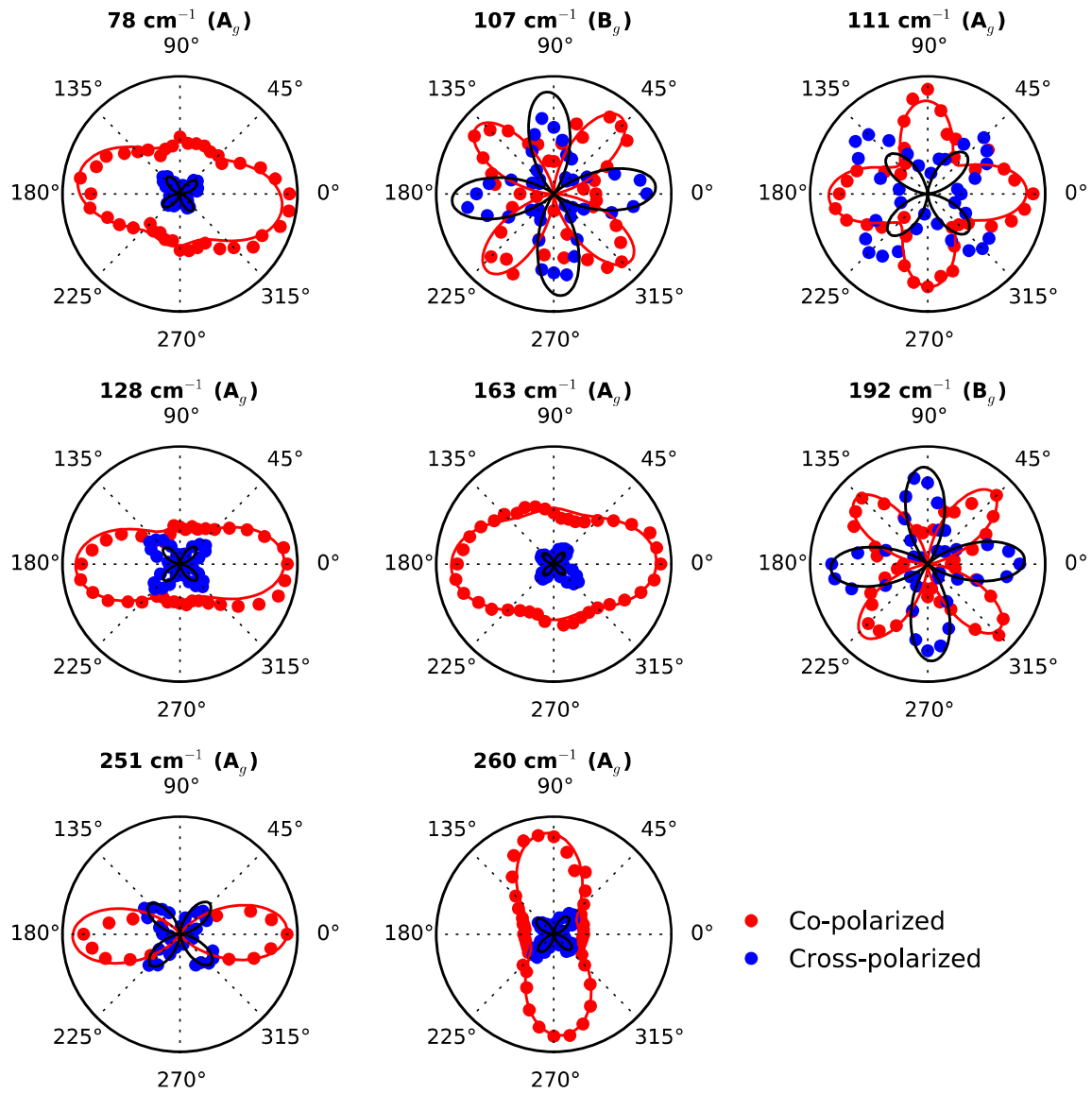


Figure S4. Raman tensor fits to the intensities of the prominent $1\Gamma'$ - MoTe_2 modes for the co-polarized (red) and cross-polarized (blue) configurations. The fits allow for assignment of symmetry.

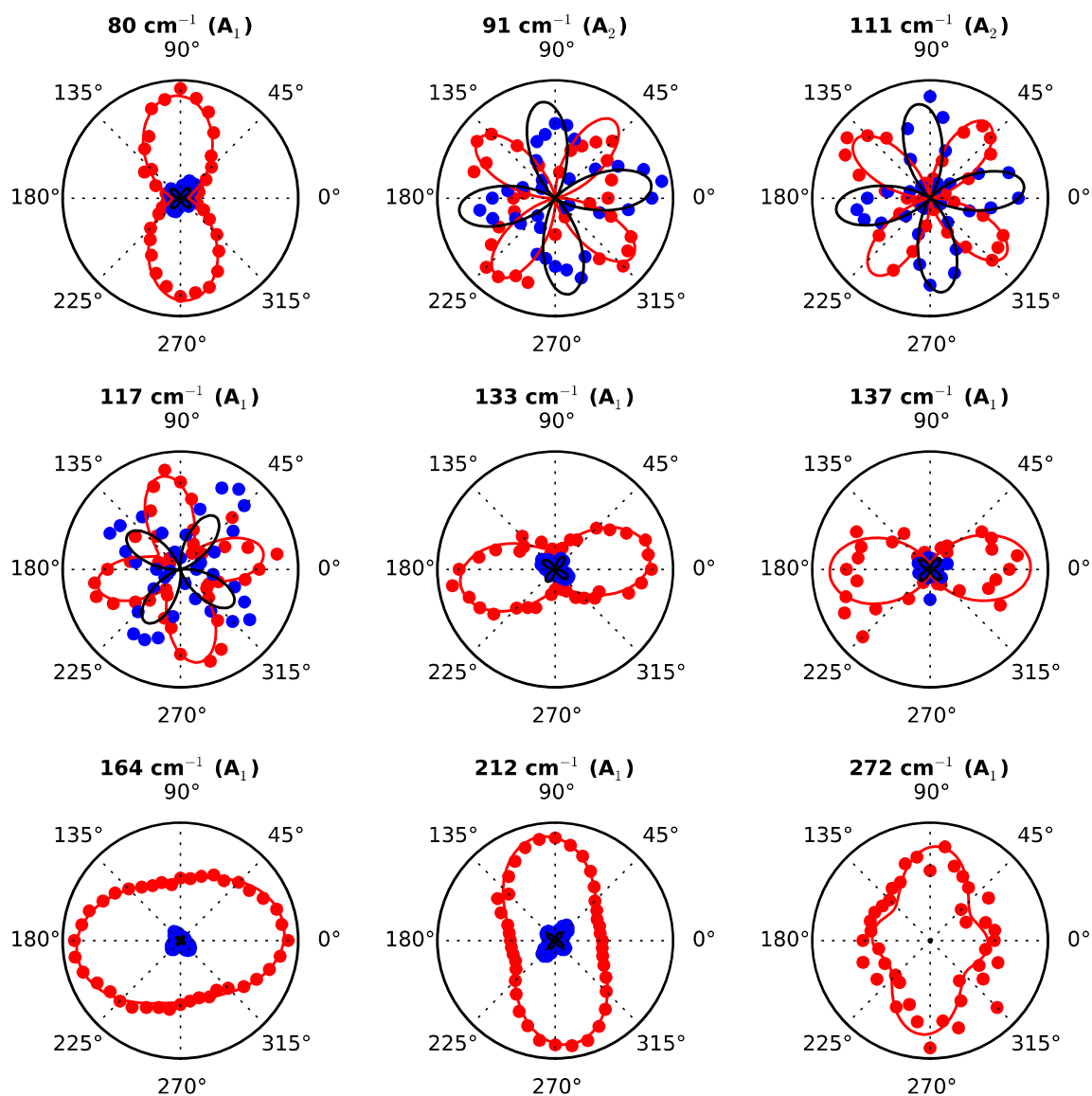


Figure S5. Raman tensor fits to the intensities of the prominent WTe_2 modes. The fits allow for the assignment of symmetry for the co-polarized (red) and cross-polarized (blue) configurations.

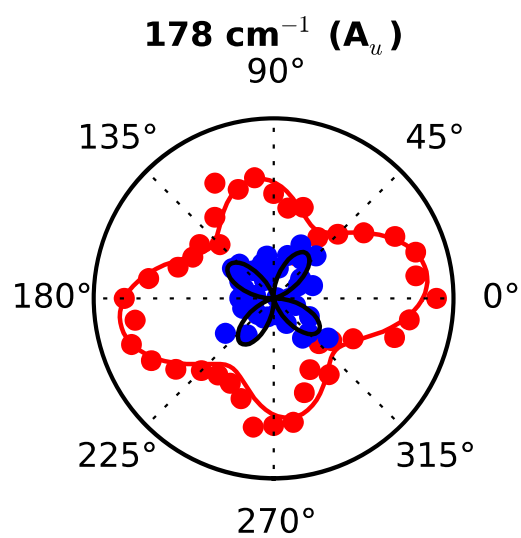


Figure S6. A Raman tensor fit to the 178 cm⁻¹ disorder peak from the $x = 0.29$ composition. This mode is unique to alloys and is highlighted in box ii of Figure 2e and Figure 3b. The peak is further analyzed in Figure 3d.

2. Supporting Note 2

Polarized Raman measurements allow a peak with intensity I to be analyzed as a function of angle between the incident and scattered light using the relation

$$I(\theta) = |\hat{e}_s \cdot \overset{\leftrightarrow}{R} \hat{e}_i|^2. \quad (\text{S1})$$

Here, \hat{e}_i is the unit vector for the direction of polarization of the incident light, $\overset{\leftrightarrow}{R}$ is the Raman tensor representing the symmetry of the peak mode, and \hat{e}_s is the unit vector for the polarization of the scattered light that is collected. In our case, we use $\hat{e}_i = \begin{pmatrix} \cos \theta & \sin \theta & 0 \end{pmatrix}$ for the incident light, and $\hat{e}_s^{\parallel} = \begin{pmatrix} \cos \theta & \sin \theta & 0 \end{pmatrix}$ or $\hat{e}_s^{\perp} = \begin{pmatrix} -\sin \theta & \cos \theta & 0 \end{pmatrix}$ for scattered light in either the co-polarized or cross-polarized configurations, respectively.

Using the given Raman tensors for point groups C_{2h} and C_{2v} , to which 1T'-MoTe₂ and WTe₂ belong, respectively, we are able to definitively assign the symmetry of the modes of the pure samples and track these modes through the alloy spectrum. Now, 1T'-MoTe₂ belongs to point group C_{2h} , and thus has the modes A_g and B_g . These modes are represented by the Raman tensors

$$A_g = \begin{pmatrix} a & 0 & d \\ 0 & b & 0 \\ d & 0 & c \end{pmatrix} \quad (\text{S2}) \quad B_g = \begin{pmatrix} 0 & f & 0 \\ f & 0 & g \\ 0 & g & 0 \end{pmatrix}. \quad (\text{S3})$$

Similarly, WTe₂ belongs to point group C_{2v} , and thus has the modes A_1 , A_2 , B_1 , and B_2 , which are represented by the Raman tensors

$$A_1 = \begin{pmatrix} a & 0 & 0 \\ 0 & b & 0 \\ 0 & 0 & c \end{pmatrix} \quad (\text{S4}) \quad A_2 = \begin{pmatrix} 0 & f & 0 \\ f & 0 & 0 \\ 0 & 0 & 0 \end{pmatrix} \quad (\text{S5})$$

$$B_1 = \begin{pmatrix} 0 & 0 & d \\ 0 & 0 & 0 \\ d & 0 & 0 \end{pmatrix} \quad (\text{S6}) \quad B_2 = \begin{pmatrix} 0 & 0 & 0 \\ 0 & 0 & e \\ 0 & e & 0 \end{pmatrix}. \quad (\text{S7})$$

We find it necessary to include a complex component in these tensors, as is typically done when accounting for the effect of light absorption by the material. This is because each element R_{ij}^k of the Raman tensors is given by the derivative of the dielectric function element ϵ_{ij} with respect to the normal coordinate q^k . The components ϵ_{ij} of the dielectric function tensor for absorptive materials have real and imaginary parts so that $\epsilon_{ij} = \epsilon'_{ij} + i\epsilon''_{ij}$. Thus, Raman tensor elements are given by $R_{ij}^k = \frac{\partial \epsilon_{ij}}{\partial q^k} = \frac{\partial \epsilon'_{ij}}{\partial q^k} + i \frac{\partial \epsilon''_{ij}}{\partial q^k}$

so that the components become, for example, $a = |a|e^{i\phi_a}$, $b = |b|e^{i\phi_b}$, and so on.

The expected intensities of the modes for the pure 1T'-MoTe₂ and pure WTe₂ were calculated using Equation (S1). It was found that the intensities of the A_g mode in pure 1T'-MoTe₂ and the A_1 mode in pure WTe₂ in both the co-polarized and cross-polarized configurations are expected to be equal so that

$$I_{A_g}^{\parallel} = I_{A_1}^{\parallel} = |a|^2 \cos^4 \theta + |b|^2 \sin^4 \theta + \frac{|a||b| \cos \phi'}{2} \sin^2 2\theta \quad (\text{S8})$$

and

$$I_{A_g}^{\perp} = I_{A_1}^{\perp} = \frac{\sin^2 2\theta}{4} (|a|^2 + |c|^2 - 2|a||c| \cos \phi') \quad (\text{S9})$$

where the phase difference ϕ' was $\phi' = \phi_b - \phi_a$ for the A_g and A_1 modes. Similarly, the expected intensity of the B_g mode in pure 1T'-MoTe₂ is found to be equal to the A_2 mode in pure WTe₂ so that

$$I_{B_g}^{\parallel} = I_{A_2}^{\parallel} = |f|^2 \sin^2 2\theta \quad (\text{S10})$$

and

$$I_{B_g}^{\perp} = I_{A_2}^{\perp} = |f|^2 \cos^2 2\theta. \quad (\text{S11})$$

The complex phase in the B_g/A_2 modes cancels when calculating the expected intensities. In pure WTe₂, the calculated intensities of the B_1 and B_2 modes are zero, indicating that they should not be visible in either configuration. Fitting the peaks measured in the co-polarized and cross-polarized configurations simultaneously allows us to definitively assign the mode symmetries of all the peaks in 1T'-MoTe₂ and WTe₂. Table 1 in the main text shows the assignment of these modes.

Supporting Information References

- [1] B. E. Brown. The Crystal Structures of WTe₂ and High-Temperature MoTe₂. *Acta Crystallographica*, 20(2):268–274, 1966.